Hannes K¿hnle, BSc

# Ion Dynamics in Nanocrystalline Fluorine Anion Conductors for Batteries

MASTER'S THESIS

to achieve the university degree of

Diplom-Ingenieur

Master's degree programme: Technical Chemistry

submitted to

Graz University of Technology

Supervisor

Univ.-Prof. Dr. rer. nat. habil. Martin Wilkening

Institute for Chemistry and Technology of Materials

Dipl.-Ing. BSc Stefan Breuer

Graz, October 2017

## Eidesstattliche Erklärung

Hiermit erkläre ich an Eides statt, dass ich die vorliegende Arbeit selbstständig verfasst, andere als die angegebenen Quellen/Hilfsmittel nicht benutzt, und die den benutzten Quellen wörtlich und inhaltlich entnommenen Stellen als solche kenntlich gemacht habe. Das in TUGRAZonline beziehungsweise UNIGRAZonline hochgeladene Textdokument ist mit der vorliegenden Diplomarbeit identisch.

## Affidavit

I declare that I have authored this thesis independently, that I have not used other than the declared sources/resources, and that I have explicitly indicated all material which has been quoted either literally or by content from the sources used. The text document uploaded to TUGRAZonline and UNIGRAZonline is identical to the present diploma thesis.

Ort, Datum / Place, Date

(Hannes Kühnle)

Unterschrift / Signature

## Acknowledgement

The realization of this diploma thesis wouldn't have been possible without the support of the following people. Thank you very much for your help and kindness:

**Univ.-Prof. Dr. rer. nat. habil. Wilkening**, for taking me into his group, the supervision and his precious advises.

**Dipl.-Ing. BSc Stefan Breuer**, for accompanying me along my diploma thesis, his kind supervision, instructions and practical advice, as well as his invaluable support.

**Ing. Veronika Pregartner**, for instructing me kindly to a variety of equipment and giving me a lot of practical advice.

**Oberrätin Dipl.-Ing. Dr.techn. Brigitte Bitschnau** and **Ao.Univ.-Prof. Dipl.-Ing. Dr.techn. Franz Mautner**, for all the XRD-measurements and support with the interpretations.

**The whole working group** for the great working atmosphere and their support when I needed it.

My special gratitude goes out to **my whole family**, for their never-ending support during my studies. Without them, I probably wouldn't have made it through the past years.

And finally, I want to thank **my friends**, who supported me during my time in Graz and made me feel like at home.

## Abstract

The currently globally focused goal of a more sustainable future, builds among others, strongly on the improvement and new development of ion-conducting systems. Due to the energy storing properties, these electrochemical systems form the basis for an ever-increasing electromobility as well as for a more efficient use of renewable energies. Within the scope of this thesis, different samples of the inverse perovskite $BaLiF_3$ (space group $Pm\bar{3}m$) were prepared by milling and tempering the binary fluorides LiF and $BaF_2$ under an argon atmosphere and were characterized for their crystallinity and ion conductivity. The samples were first synthesized mechanochemically using high-energy ball milling, to gain material properties, which are not or only difficult to achieve via conventional high-temperature synthesis. Subsequently, parts of the mechanochemically prepared products were thermally treated to investigate the influence of the heat treatment. The crystallographic properties were determined via X-ray diffraction measurements, to compare the reaction conversion and the crystallinity. Impedance spectroscopy was employed, to determine the dielectric properties and the ion conductivity. Finally, the samples were investigated by nuclear magnetic resonance (NMR), to characterize the $^{7}$Li- and $^{19}$F-ion dynamics as a function of the temperature.

## Kurzfassung

Das derzeit weltweit fokussierte Ziel einer nachhaltiger gestalteten Zukunft, baut unter anderem maßgeblich auf die Verbesserung und Neuentwicklung ionenleitender Systeme. Auf Grund der energiespeichernden Eigenschaften, stellen diese elektrochemischen Systeme die Basis für eine immer stärker aufstrebende Elektromobilität als auch für eine effizientere Nutzbarmachung von erneuerbaren Energien dar. Im Rahmen dieser Diplomarbeit wurden unterschiedliche Proben des inversen Perovskits $BaLiF_3$ (Raumgruppe $Pm\bar{3}m$) durch Mahlen sowie anschließendes Tempern der binären Fluoride LiF und $BaF_2$ unter Argonatmosphäre hergestellt und die jeweiligen Materialien auf ihre Kristallinität und ionische Leitfähigkeit hin untersucht. Die Proben wurden zunächst mechanochemisch durch Hochenergiekugelmahlen dargestellt, um Materialeigenschaften zu erhalten, welche über konventionelle Hochtemperatursynthesen nicht oder nur schwierig zu erzeugen sind. Anschließend wurden Teile der mechanochemisch erzeugten Produkte thermisch behandelt, um den potentiellen Einfluss der Wärmebehandlung nachvollziehen zu können. Die kristallographischen Eigenschaften wurden mittels Röntgendiffraktometrie bestimmt, um den Reaktionsumsatz und die Kristallinität vergleichen zu können. Impedanzspektroskopie wurde verwendet, um die dielektrischen Eigenschaften und die ionische Leitfähigkeit ermitteln zu können. Abschließend wurden die Proben mittels statischer Kernspinresonanz (NMR) untersucht, um die Dynamik der $^{7}Li$- und $^{19}F$-Ionen in Abhängigkeit von der Temperatur charakterisieren zu können.

# Content

# 1 Introduction

Due to their fast ion conduction, nanocrystalline ceramics play a more and more important role in the development of modern electrochemical systems. They are applied for instance in the development of energy storage solutions (smart power grids) for sustainable energy sources such as solar, wind and water power, in battery systems for the electromobility industry as well as in mobile devices like laptops, cameras and phones [1–5]. Ongoing research still has the continuous aim to increase the conductivity properties of existing systems [6] or even tries to develop new energy storage systems [7, 8].

One way to prepare new ceramic materials is given by using high-energy ball milling, which often shows a change in properties, such as increased ionic conductivity, compared to their microcrystalline equivalents [9]. This simple method allows the synthesis of defect-rich nanocrystalline powders, which would not be accessible through conventional high-temperature or wet chemical synthesis. Furthermore, this method allows it to carry out product formation at low temperatures, which reduces the loss of volatile compounds as well as the required energy input [10, 11].

Presumably, the two mobile carriers $Li^+$ and $F^-$ are present in the inverted perovskite $BaLiF_3$ in contrast to $LiTaO_3$, where Li cations are dominating the ionic conductivity [12]. The collected data of this thesis could give insights about the ionic mobility of $BaLiF_3$.

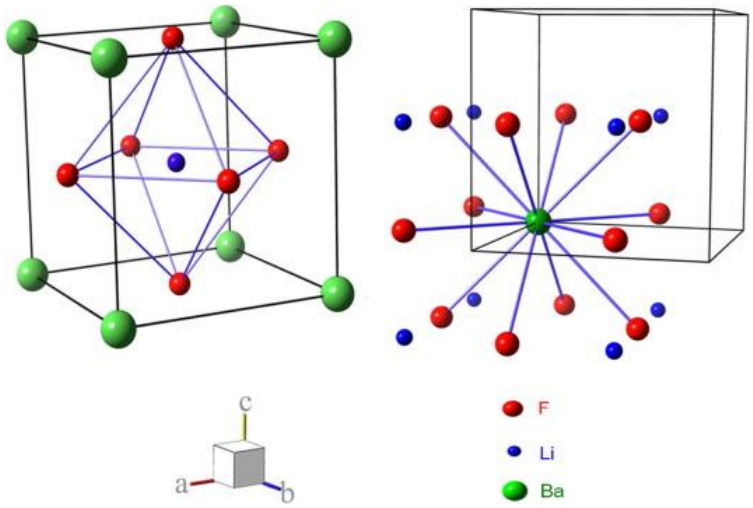


**Fig. 1.1** Co-ordination sphere for cations in $LiBaF_3$ 8-coordination of $Li^+$ and 12-coordination of $Ba^{2+}$ are depicted [52]. The scheme was taken from [52].

# 2 Fundamentals

## 2.1 Diffusion in solids

### 2.1.1 Fundamentals of Diffusion

The word diffusion, which is deviated from the Latin word *diffundere* (engl. 'to spread out'), describes the movement of particles in gases, liquids and solids from a region of a high concentration (or high chemical potential) to a region of a lower concentration (or lower chemical potential) [13]. The driving force is the entropy. In contrast to gases and liquids, where particles can migrate almost freely between a non-orientated matrix, diffusion in solids takes place in a dense and well-defined lattice structure [14].

For an ideal crystal, there are 14 possible arrangements with well-defined positions for each atom, which are called *Bravais-lattices*. However, in real crystal structures, the well-defined crystal structure is disturbed by a variety of defects. These defects are necessary, that solid ion diffusion can take place [14]. The diffusion takes place by *hopping* of mobile ions (***Fig. 2.1***) from certain occupied lattice sites to neighbored vacancies or interstitial positions [15]. A closer look on the nature of point defects will be taken in the next chapter.

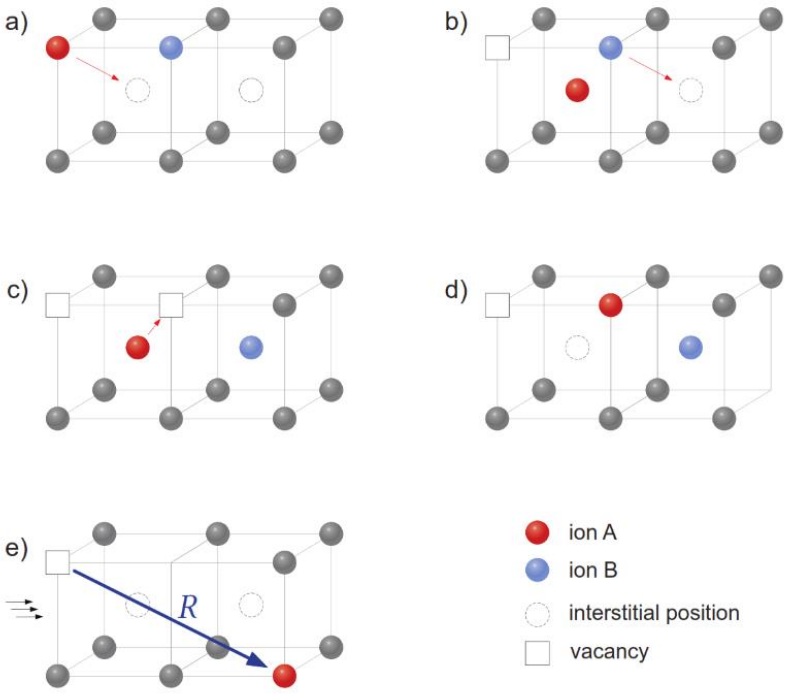


**Fig. 2.1** Illustration of the migration mechanism of an ion in a solid material which is known as the *random walk* [14]. It was taken from [14].

The mathematical description of the solid state diffusion is given by *Fick's first law* and describes the one-dimensional flux of particles in an isotropic medium (x-direction) [16]:

$$J_x = -D\frac{\partial C}{\partial x} \qquad (2.1)$$

Here, $J_x$ stands for the flux of particles (diffusion flux) and C for the concentration. The negative sign in Eq. (2.1) indicates contrary directions of diffusion flux and concentration gradient. $D$ represents the *diffusion coefficient* or the so-called *diffusivity* of the considered species. It is defined as the number of particles passing through a unit area per unit time and bear the units $[cm^2s^{-1}]$ or $[m^2s^{-1}]$. Using a vector notation, *Fick's first law* can be generalized to three dimensions:

$$\vec{J} = -D\nabla C \qquad (2.2)$$

$\vec{J}$, the vector of the flux diffusion, is directed in the counter direction to the concentration gradient vector $\nabla C$. The *nabla* symbol, $\nabla$, expresses the vector operation on the right-hand side of Eq. (2.2), acts on the scalar concentration field $C(x, y, z, t)$ and forms the concentration gradient field $\nabla C$ [16]. The vector of the concentration gradient always faces in the direction, in which the concentration field undergoes the most rapid increase [16].

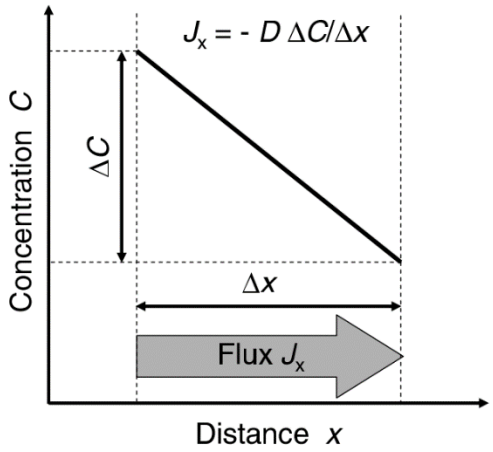


**Fig. 2.2** Illustration of Fick's first law. It was taken from [15].

Using an arbitrary point P with the coordinates $(x, y, z)$ in a volume of $(\Delta x, \Delta y, \Delta z)$ (***Fig. 2.3***) and using the fact, that the diffusion flux $\vec{J}$ and its components $J_x, J_y, J_z$ vary across the volume, a material balance can be expressed as:

$$material\ inflow - material\ outflow = accumulation/loss\ rate.$$

The mathematical expression of this material balance is

$$[J_x(P) - J_x(P + (\Delta x)]\Delta y\Delta z + [J_y(P) - J_y(P + (\Delta y)]\Delta x\Delta z + [J_z(P) - J_z(P + (\Delta z)]\Delta x\Delta y = accumulation/loss\ rate \quad (2.3)$$

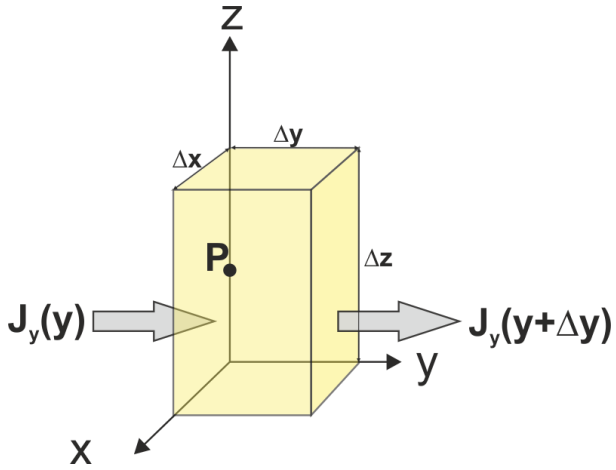


**Fig. 2.3** Representation of an infinitesimal test volume according to [16]. The in- and outgoing diffusion flux of the y-component are indicated by the arrows. The diffusion flux for the x- and z-component can be analogously applied to the y-direction [16].

The terms in the square brackets can be replaced by $\frac{\Delta x \partial J_x}{x\partial}$, $\frac{\Delta y \partial J_y}{y\partial}$ and $\frac{\Delta z \partial J_z}{z\partial}$, using Taylor expansions of the flux components in their linear forms. This leads to

$$-\left[\frac{\partial J_x}{x\partial} + \frac{\partial J_y}{y\partial} + \frac{\partial J_z}{z\partial}\right]\Delta x\Delta y\Delta z = \frac{\partial C}{\partial t}\,\Delta x\Delta y\Delta z \quad (2.4)$$

For an infinitesimal size of the volume, Eq. ( 2.4) can be written in a more compact form, using the vector operation *divergence* ∇. This vector operation acts on the vector of the diffusion flux and leads to the so called *continuity equation* [16]:

$$-\nabla \cdot \vec{J} = \frac{\partial C}{\partial t} \quad (2.5)$$

By combining *Fick's first law* Eq. ( 2.2) and the *continuity equation* Eq. ( 2.5), *Fick's second law* or the so-called *diffusion equat*ion can be obtained:

$$\frac{\partial C}{\partial t} = \nabla \cdot (D^{tr}\nabla C) \quad (2.6)$$

Due to an anisotropic diffusion, *D* is now expressed as a tensor $D^{tr}$, the so-called *tracer diffusion coefficient*. For tracer diffusion in chemically homogenous systems or ideal solid solutions, the diffusivity is concentration-independent and Eq. ( 2.6) can be simplified to the *linear diffusion equation*

$$\frac{\partial C}{\partial t} = D^{tr}\Delta C \qquad (2.7)$$

with Δ as the *Laplace operator* ($\nabla^2$). The equation can be solved by applying certain initial and boundary conditions [16]. With the help of an Arrhenius relationship, the temperature dependence of the tracer diffusion coefficient ($D^{tr}$) can be described as

$$D^{tr} = D_0^{tr}\exp(-\frac{E_A}{k_B T}) \qquad (2.8)$$

$D_0^{tr}$ stands for the pre-exponential factor, $E_A$ for the activation energy and $k_B$ for the Boltzmann constant [14].

### 2.1.2 Essential mathematical relations for solid ion diffusion

From a microscopic view, *self-diffusion* occurs by the *Brownian motion* of atoms or molecules. But on an elementary point of view, the diffusion results from many individual displacements (jumps) of the diffusing particles. These single-atom jumps have a fixed length, depending on the lattice parameters. With that knowledge, the diffusivity can be expressed as physical quantities, describing these elementary jump processes. The three quantities are the jump rate ω, the jump distance of the ions $d$ and the correlation factor $f$. Einstein and Smoluchowski connected the mean square displacement of particles $\langle R^2 \rangle$ (***Fig. 2.1***) to the diffusion coefficient $D^{sd}$. The *Einstein- Smoluchowski* relation

$$D^{sd} = \frac{\langle R^2 \rangle}{6\tau} \qquad (2.9)$$

with τ as the mean residence time of an ion at a given site, describes an uncorrelated diffusion process, which is also known as the *random walk* (see ***Fig. 2.4***). For an uncorrelated random walk of ions between neighboring vacancies in a cubic lattice and $d$ as the jump distance, the *Einstein- Smoluchowski* relation can be simplified to

$$D^{sd} = \frac{d^2}{6\tau} \qquad (2.10)$$

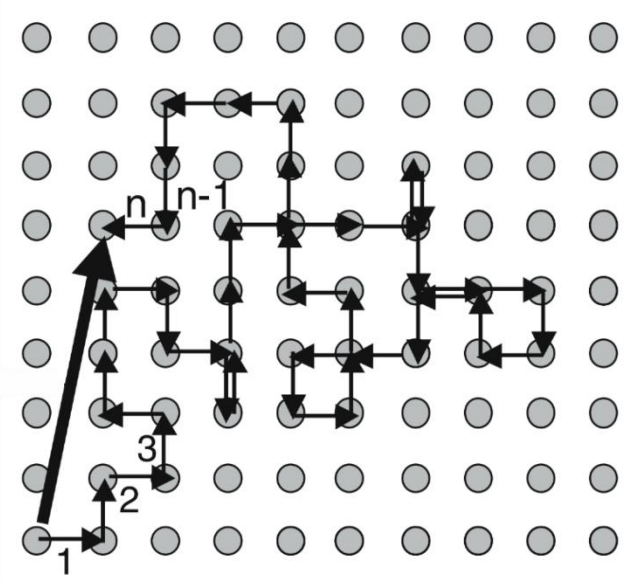


**Fig. 2.4** The illustration was taken from [16], showing an example for a random walk of a particle in a lattice.

The macroscopic ($D^{sd}$) and the microscopic ($D^{tr}$) diffusion coefficients can be connected via a correlation factor $f$, with possible values between 0 and 1 [16]:

$$D^{tr} = f \cdot D^{sd} \tag{2.11}$$

Furthermore, the Nernst-Einstein-relation

$$D^{\sigma} = \frac{\sigma_{DC} k_B T}{N q^2} \tag{2.12}$$

with $D^{\sigma}$ standing for the *charge diffusion coefficient* (also called the *conductivity diffusion coefficient*), $\sigma_{DC}$ for the *direct current ion conductivity*, $N$ for *the effective density of mobile ions* and $q$ for the ion charge, should be mentioned. This mathematical expression relates $D^{\sigma}$ and the *mobility* of the diffusing particles and is another fundamental relation for impedance spectroscopy [16].

### 2.1.3 Temperature dependence of the ion diffusion

As already mentioned, solid state diffusion in fast ionic conductors is induced by ions, which jump from occupied lattice sites to the nearest neighbored vacancies or interstitial positions [16]. The two main diffusion mechanisms are therefore called vacancy mechanism and interstitial mechanism [15]. The jump process takes place in an energy landscape indicated by

the potential curves in ***Fig. 2.5***. At constricted temperatures, the ions in the crystal lattice oscillate with moderate frequencies around their equilibrium positions (I). At this point, the activation energy is usually not high enough, to jump from one site (I) to another (II) over the saddle-point barrier $G^M$. The *Gibbs free energy of migration* of the ions $G^M$ can be expressed as

$$G^M = H^M - TS^M \qquad (2.13)$$

with $H^M$ as the *enthalpy of migration* and $S^M$ as the *entropy of migration*.

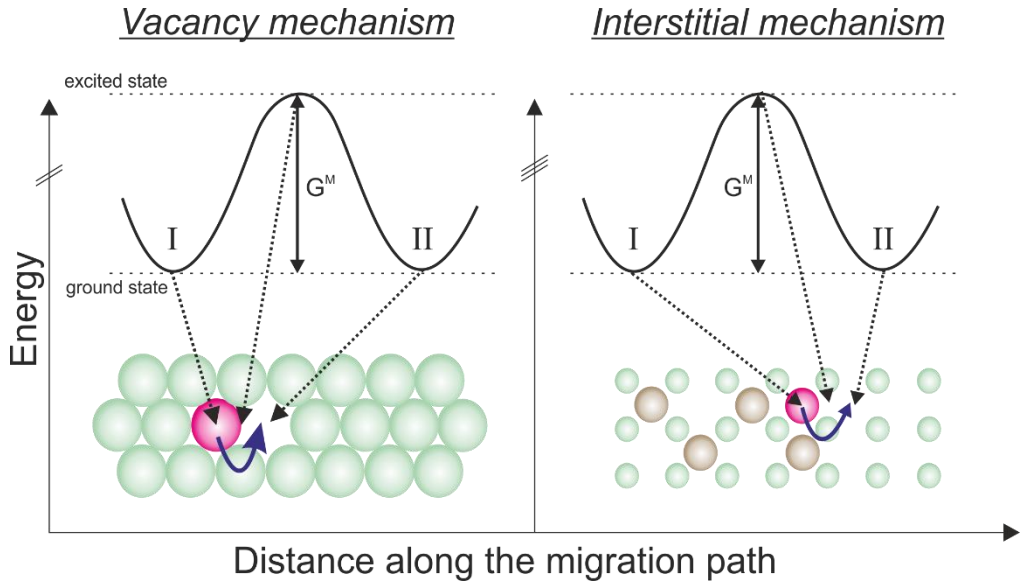


**Fig. 2.5** (left) Schematic representation of the vacancy mechanism. If enough energy is available to overcome the energy barrier ($G^M$, Gibbs free energy of migration), the redly marked ion jumps from its lattice site (I) to a neighbored vacancy site (II). The lower dashed line represents the energy level of the red ion's ground state and the upper dashed line represents the energy level of the ion while breaking through the energy barrier. (right) Analogous to the vacancy mechanism, in the interstitial mechanism, the red interstitial ion jumps to a neighbored interstitial site [16]. Schematic representation according to [16].

By employing statistical thermodynamics, the *jump rate* ω (number of jumps per unit time to a neighboring site) can be expressed as

$$\omega = \nu^0 \exp\left(-\frac{G^M}{k_B T}\right) = \nu^0 \exp\left(-\frac{S^M}{k_B}\right) \exp\left(-\frac{H^M}{k_B T}\right) \qquad (2.14)$$

where $\nu^0$ is called the *attempt frequency*. It can be understood as the vibration frequency at the equilibrium state but in the direction of the reaction path [16]. At a given temperature, the ions have a finite probability of jumping out of their lattice sites. The probability is proportional to $\exp\left(-\frac{H^M}{k_B T}\right)$, which means, that the probability of a successful jump increases with an

increasing temperature. By using a one-dimensional model for the jump diffusion (***Fig. 2.6***), this also means, that a successful ion jump in the forward and backwards direction will have the same probability.

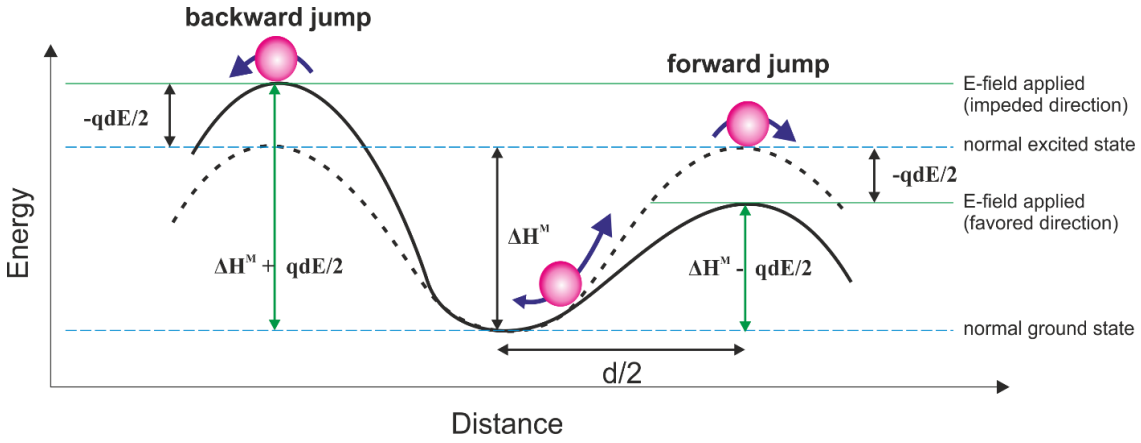


**Fig. 2.6** One dimensional model for jump diffusion in ionic conductors according to [16].

Assuming, the vibration of the ions can be described as a harmonic oscillator, the attempt frequency $\nu_0$ can be estimated to be of the order of

$$\nu_0 \sim \left( \frac{\sqrt{\frac{\Delta H^M}{M}}}{d} \right) \qquad (2.15)$$

with $M$ as the reduced mass of the oscillator and $d$ as the jump distance. In the absence of an electric field $E$, the activation energy of the ion hopping is always $\Delta H^M$ and the jump frequency ω for forward and backwards jumps will be the same. Applying an electric field $E$, the jump frequency in one direction can be favored and will increase Eq. (2.16). The activation energy is decreased by $qdE/2$. With $q$ as the electric charge of the hopping ions and $d$ as the jump distance. Analogous, the opposite jumping direction is hindered by the electric field Eq. (2.17), due to an increase of the activation energy by $qdE/2$ [15].

$$\omega = \nu^0 \exp\left(-\frac{S^M}{k_B}\right) \exp\left(-\frac{H^M - qdE/2}{k_B T}\right) \qquad (2.16)$$

$$\omega = \nu^0 \exp\left(-\frac{S^M}{k_B}\right) \exp\left(-\frac{H^M + qdE/2}{k_B T}\right) \qquad (2.17)$$

## 2.2 The nature of defects

Energy is always required to form defects in crystals, which is why the formation is always an endothermic process. The quantity $\Delta G = \Delta H - T\Delta S$ denotes the overall change in the free energy of the crystal and is pictured in ***Fig. 2.7***. It might be surprising, but defects exist in crystals, even though in very small concentrations. The driving force is a gain in entropy coming along with the formation of these defects [17].

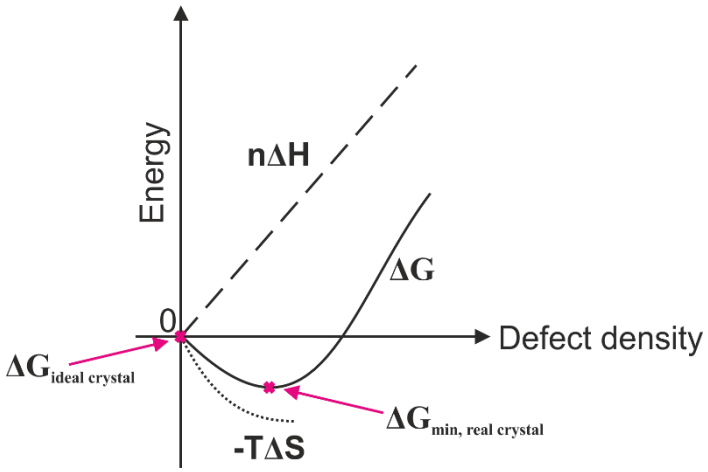


**Fig. 2.7** Relation between the defect density and the Gibbs free energy in a crystal. Increasing the temperature introduces more defects for an endothermic reaction (Le Chatelier's principle). Scheme according to [53].

In an ideal crystal, an idealized model without any impurities, all ions have their determined places in the lattice. The building units of the crystal are translationally invariant and belong to one of the 230 space groups [18]. Due to the number of accessible microstates are correlating with the entropy, at absolute zero (0 K) the system is in a unique zero energy state with an entropy equal to zero ($\Delta G_{ideal\ crystal}$) [19]. However, in real crystals a variety of defects, such as point, line and area defects, can be present. Point defects are stabilized, because they are connected to a thermodynamic equilibrium (***Fig. 2.7***, $\Delta G_{real\ crystal}$) [20]. ***Fig. 2.7*** illustrates, that moving from absolute zero to higher temperatures, the system can lower its total energy $\Delta G$, until it reaches a minimum ($\Delta G_{min,real\ crystal}$). At this thermodynamically stable point, the entropy is unequal zero which means that a number of accessible microstates, and therefore a number of defects, are present. To further increase the number of defects in the system, energy in form of heat must be introduced.

For real crystals, the *Gibbs energy of the vacancy formation* is defined as the corresponding change of the *Gibbs energy of the whole crystal* $\Delta G$. If $n$ atoms are removed from the crystal containing $N$ atom sites, each $n$ vacancies will be associated with the enthalpy of formation $H_F$.

The formation of the vacancies induces a disturbance of the neighbors of the vacancies and leads also to the formation of a vibrational entropy $S_F$.

Additionally, a configurational entropy $S_C$ appears, which is equal to

$$S_C = k_B \ln[\frac{(N+n)!}{N!\,n!}] \quad (2.18)$$

By subtracting both entropies $S_F$ and $S_C$ from $H_F$, the whole change of the Gibbs energy of the crystal is given by [21]:

$$\Delta G = nH_F - TS_C - nTS_F \quad (2.19)$$

Due to the equation describes an endothermic reaction, increasing the temperature increases also the number of defects (Le Chatelier's principle) [17].

## 2.3 Point defects in ceramics

Even if the word *defect* has a negative meaning in the common parlance, many important applications like luminescence, diffusion and mechanical properties would not even be possible without *crystal defects* [18]. The ions in simple ionic crystals are mobile due to the presence of site disturbing point defects [16]. They can be separated into two groups: intrinsic and extrinsic point defects.

### 2.3.1 Intrinsic point defects

Intrinsic defects do not change the overall composition of the crystal, why they are also known as stoichiometric defects [17]. Two main intrinsic defects are known in 1:1 MX solids (***Fig. 2.8***), such as rock salt (NaCl), wurtzite (ZnS) and caesium chloride (CsCl) [22]. A **Schottky defect** consist of a pair of vacant sites, an equal number of cation and anion vacancies to preserve electroneutrality. It occurs, when ions are leaving their lattice sites and migrate to the crystal surface. A Schottky defect for a $MX_2$-type material would be composed of a vacancy caused by an $M^{2+}$ cation and *two* $X^-$ anion vacancies. If anions migrate to interstitial sites and thereby creating vacancies in the lattice, the defect is called a **Frenkel defect** [18]. It usually only occurs on a sublattice of a crystal. In silver chloride (AgCl) for example *cation Frenkel defects* can be observed, where $Ag^+$ ions migrate from their octahedral coordination sites into tetrahedral coordination. In general, it is less common to observe *anion Frenkel defects*, because anions are usually larger than their counter ions in the structure. An exception is calcium

fluoride ($CaF_2$), where an array of close-packed (ccp) $Ca^{2+}$ ions has all tetrahedral sites completely occupied by small $F^-$ ions. The $F^-$ ions can now move through the relatively larger $Ca^{2+}$ structure to the unoccupied and larger octahedral holes [17].

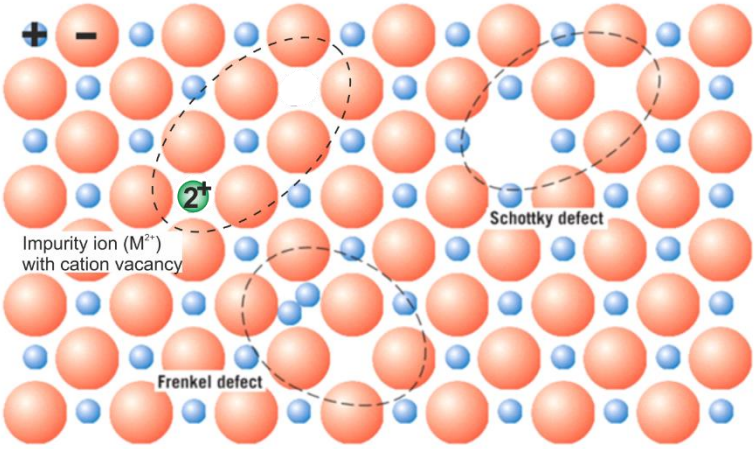


**Fig. 2.8** The schematic diagram was taken from [22] and information was added. It shows Frenkel and Schottky defects as well as an introduced impurity ion with a cation vacancy in an ionic solid.

### 2.3.2 Extrinsic point defects

Extrinsic defects are created when dopants with a different charge get introduced into a crystal lattice [16, 22]. If this is done by purpose, the process is called **doping**. For interstitial defects, the ion radius of the impurity should be relatively small in comparison to the atom radius giving the lattice structure. Because both, cations and anions are present in a ceramic material, a substitutional impurity will substitute the host ion which is most like its own electrical charge. By introducing calcium chloride ($CaCl_2$) into rock salt (NaCl), *one* $Ca^{2+}$ ion replaces *two* $Na^+$ ions. The doping of the rock salt creates one artificial cation vacancy to maintain electrical neutrality (***Fig. 2.8***) [17].

## 2.4 X-ray-diffraction (XRD)

Diffraction occurs when a wave encounters a regular spaced structure which is capable of scattering the wave and has spacings which are from the same magnitude as the wavelength. Furthermore, diffraction is the consequence of phase relationships between two or more waves that have been scattered by the obstacle. The interaction between these waves can be either from a constructive or deconstructive nature (***Fig. 2.9***). If two monochromatic waves (wave 1

and 2) with the wavelength λ get scattered on an obstacle and remain in phase (wave 1' and 2'), their amplitudes add up to a stronger signal. This phenomenon is called constructive interference. The opposite phenomenon takes place, when two monochromatic waves (wave 3 and 4) with the wavelength λ get scattered on an obstacle and get out of phase (wave 3' and 4'). Then destructive interference takes place and their amplitudes cancel each other out. Phase relationships in-between these two extremes exist but result in less intense interference [22].

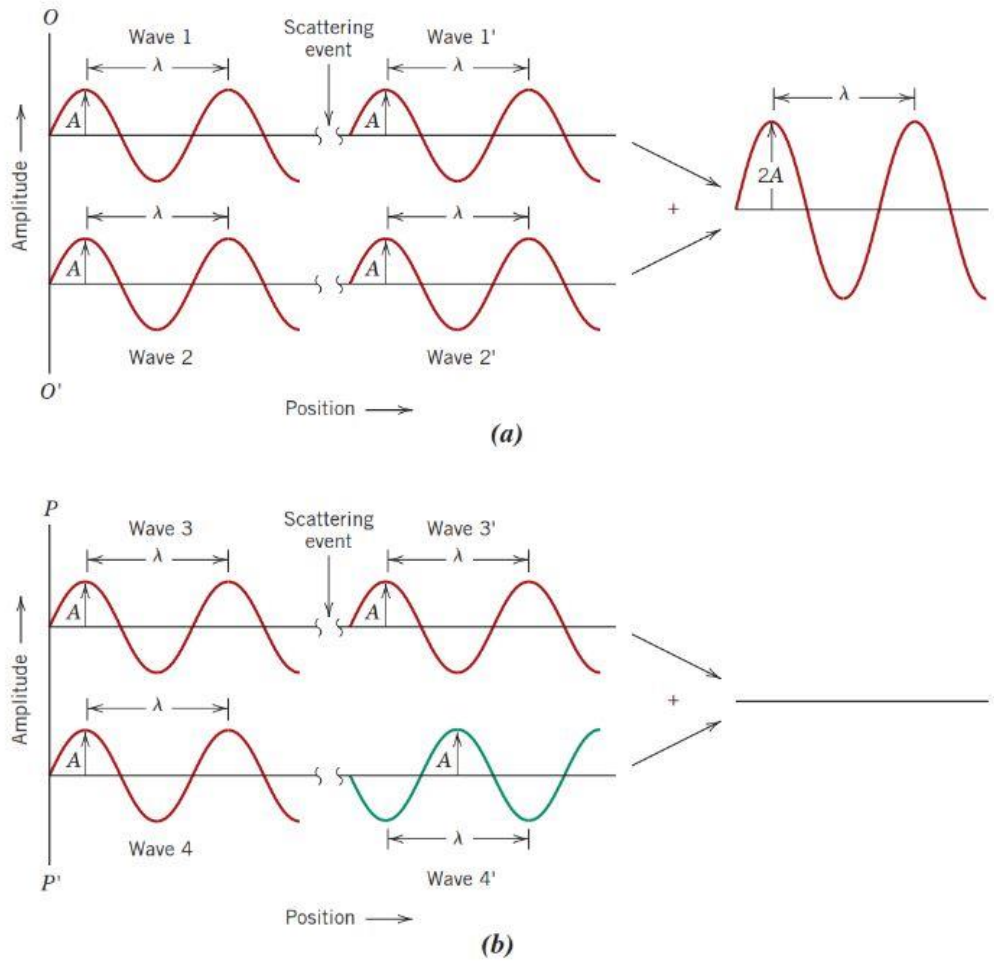


**Fig. 2.9** The schematic illustration was taken from [22]. (a) shows how two monochromatic waves with the wavelength λ (wave 1 and 2) remain in phase (wave 1' and 2') after a scattering event and constructively interfere with each other. (b) shows how two monochromatic waves with the wavelength λ (wave 3 and 4) become out of phase (wave 3' and 4') after a scattering event and destructively interfere with each other. Being out of phase, the amplitudes of the waves 3' and 4' cancel each other out.

A lattice plane can have cross sections with the axis *a*, *b* and *c* of a coordinate system. By referring the three possible cross sections named *m*, *n* and *p* (***Fig. 2.10***) to a plane, it can be clearly determined. The reciprocal values $\frac{1}{m}, \frac{1}{n} and \frac{1}{p}$ are called *h*, *k* and *l* and are known as the *Miller indices*. The indices (hkl) are used to characterize the orientation of a layer.

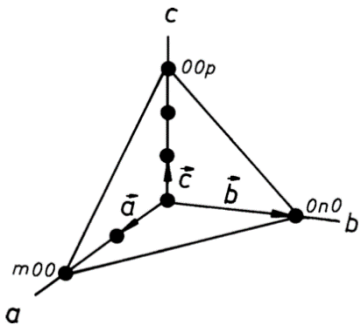


**Fig. 2.10** The scheme was taken from [18] showing the axis or a coordinate system and the coordinates of a general lattice plane (m, n, p).

To understand how X-ray diffraction works, the scattering of the electromagnetic waves on a regularly spaced structure can be considered as two parallel planes of atoms (A-A' and B-B') which have the same *h*, *k* and *l* Miller indices (***Fig. 2.10***) and are separated by the interplanar spacing $d_{hkl}$ (***Fig. 2.11***). A X-ray source generates a beam of parallel, monochromatic and coherent X-rays with the wavelength λ, which is incoming at an angle θ. For a better clarification, only two waves are representing the whole X-ray radiation [22].

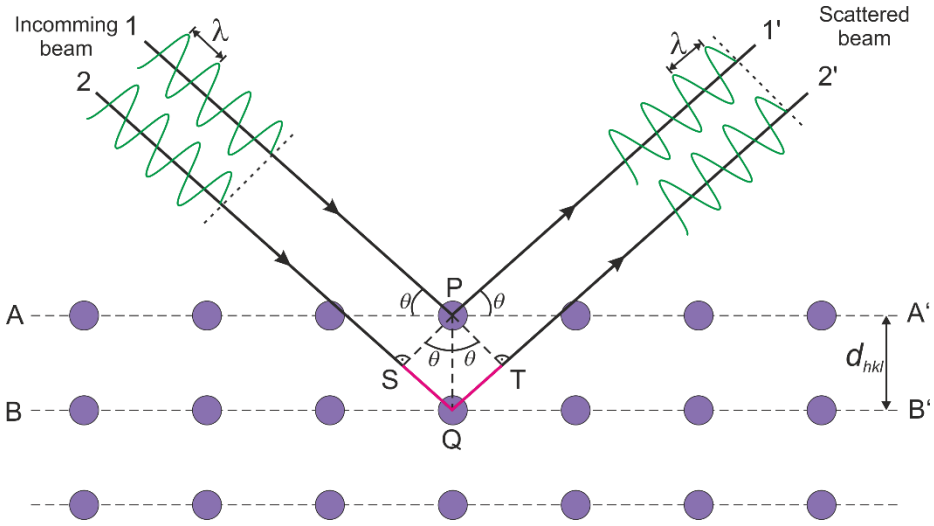


**Fig. 2.11** Schematic drawing of parallel, monochromatic and coherent X-rays getting scattered by layers of atoms according to [22]

The two incoming X-ray beams (1 and 2) hit the atoms *P* and *Q* and get scattered. The structure determines the phase relation between the two outgoing beams (1' and 2'). If the path length of the X-rays (1-P-1' and 2-Q-2') differs by a whole multiple *n* of the wavelength, constructive interference takes place [22].

A mathematical relation can be derived by comparing the difference in path length between the two rays

$$\Delta\ path\ length\ between\ beam\ 1\ to\ 2 = \overline{SQ} + \overline{QT} \quad (2.20)$$

And it is also true that

$$\overline{SQ} = \overline{QT} = d_{hkl} sin\theta \quad (2.21)$$

Now, the whole difference in the path length can be written as two times $\overline{SQ}$ (or two times $\overline{QT}$). By combining ( 2.20) and ( 2.21), the relation

$$\Delta\ path\ length\ between\ beam\ 1\ to\ 2 = 2\overline{SQ} = 2d_{hkl} sin\theta \quad (2.22)$$

can be written down. To get constructive interference, the two X-ray beams must be in phase which is only possible when the difference in path length is equal to a number of *n* (( 2.23)).

$$n\lambda = 2d_{hkl} sin\theta \quad (2.23)$$

This condition was stated first in 1912 and is called the **Bragg's law**. It relates the spacing between the lattice planes ($d_{hkl}$) to a particular **Bragg angle** ($\theta$) for each set of planes [17]. The magnitude of interplanar spacing ($d_{hkl}$) is also a function of the Miller indices for the planes. To point out two important plane-spacing equations, ( 2.24)

$$d_{hkl} = \frac{a}{\sqrt{h^2 + k^2 + l^2}} \quad (2.24)$$

is used for *cubic systems* with the lattice parameter *a*, and ( 2.25)

$$d_{hkl} = \frac{a}{\sqrt{\frac{3}{4}(h^2 + hk + k^2) + l^2(a^2/c^2)}} \quad (2.25)$$

is used for *hexagonal systems* with the lattice parameters *a* and *c* [23]. By combining The Braggs law and the plane spacing equation for a cubic crystal system, the equation

$$sin^2\theta = \frac{\lambda^2}{4a^2}(h^2 + k^2 + l^2) \quad (2.26)$$

is the result. It predicts all possible Bragg angles at which diffraction can occur from the planes (*hkl*) for a given wavelength and a cubic system with the unit cells size *a* [24]. There are two experimental main setups to measure X-ray diffractograms, the **Bragg-Brentano-**

**configuration** (angles measured in $2\theta$) and the **Debye-Scherrer photographic method** (angles measured in $4\theta$) [18]. The angles are recorded as a multiples of $\theta$, which is why the measured angles are referred to as the **diffraction angles** [23].

X-ray diffractometers with a known wavelength can be used to determine the scattering angles and the spacing between the crystal planes of an unknown specimen (***Fig. 2.12***). If the specimen is a single crystal, the scattering process takes place on a well-orientated crystal lattice. All lattice planes have the same orientation which is why the constructively interfering and scattered rays will have all the same direction. This is why the measured reflection pattern on the film, will appear as single sharp spots (***Fig. 2.13***, (1)).

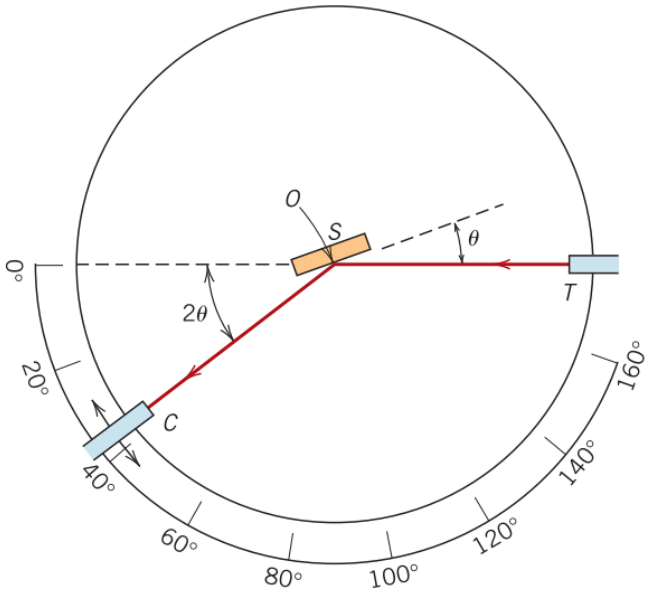


**Fig. 2.12** The schematic diagram was taken from [22], shows an X-ray diffractometer; *T* = X-ray source, *S* = specimen, *C* = detector, and *O* = axis around which the specimen and detector rotate.

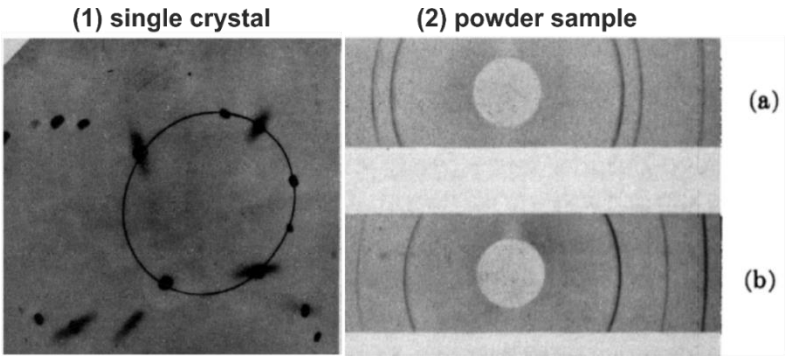


**Fig. 2.13** The XRD-patterns were taken from [24]. (1) Transmission Laue pattern of an aluminum single crystal (cubic) marked with a black circle. (2) Debye-Scherrer powder pattern of (a) copper (FCC) and (b) tungsten (BCC).

Using a powder sample and not a single crystal, a variety of randomly orientated smaller crystals is present in the sample. The crystallites have the same lattice structure as the single crystal but their individual lattice planes point in many different directions. The constructively interfering and scattered rays point now in many directions. Rotating the sample during a measurement on a plate by 360 °, not just single spots but circular patterns at the same angle will appear on the film (***Fig. 2.13***, (2)) [24].

The obtained XRD-patterns will be plotted as the reflection intensity [*a. u.*] versus the diffraction angle [2 $\theta$]. In 1956, microphotometers were used to plot the powder pattern in an analog way. Today, all data is handled digitally of course, but taking a look at this old method helps a lot for the understanding of the procedure (***Fig. 2.14***) [24].

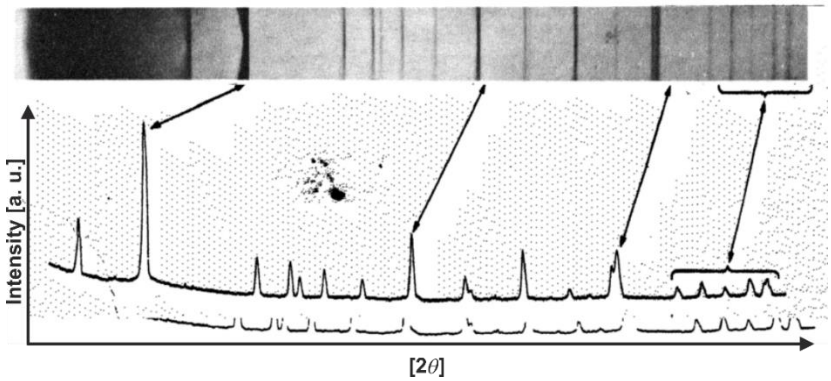


**Fig. 2.14** the photograph was taken from [24] and was edited. It shows a X-ray powder pattern of quartz (top) and the corresponding microphotometer trace (bottom).

To determine the mean crystallite size $D_{hkl}$, Scherrer's equation [25] is used

$$D_{hkl} = \frac{K\lambda}{B_{hkl}cos\theta} \qquad (2.27)$$

where $D_{hkl}$ is the crystallite size vertically to the lattice planes, *hkl* are the Miller indices of the analyzed planes, $K$ is a numerical factor referred to as the crystallite-shape factor, $\lambda$ is the used wavelength, $B_{hkl}$is the width (full-width at half-maximum) of the X-ray reflection in radians and $\theta$ as the Bragg angle. In the absence of detailed shape information, $K$= 0.9 is a good approximation. It is also important, that Scherrer's equation is only applicable for an average crystallite size of 100 – 200 nm, because reflection broadening decreases with an increasing crystallite size. It becomes difficult to separate reflection-broadening caused by the crystallite size from the broadening introduced by other factors [25]. Next to the crystallite size another

main factor for the reflection broadening is the microstrain or lattice strain $\varepsilon$. The micro strain can be described by

$$\varepsilon = \frac{\Delta d_{hkl}}{d_{hkl}} \quad (2.28)$$

with $\Delta d_{hkl}$ as the difference between the lattice-plane spacing in a strained crystal system ($d_{hkl}$) and the difference between the lattice-plane spacing in a non-strained reference crystal system ($d_{hkl,0}$) [26].

## 2.5 Electrochemical Impedance Spectroscopy (EIS)

Electrochemical impedance spectroscopy (EIS), or just impedance spectroscopy (IS), is a powerful tool to characterize electrochemical properties of materials. It can be used to analyze mass transport, chemical reaction rates, corrosion, dielectric properties, defects and the microstructure of solids. It is very helpful to predict the performance of a variety of applications, such as chemical sensors and fuel cells [27].

### 2.5.1 The General concept of the Impedance Spectroscopy (IS)

Electrons moving through conductors experience some degree of friction or counterforce under most conditions. This hindrance of motion is called resistance. A basic way to describe such electric circuits is the Ohm's Law

$$V = R \cdot I \quad (2.29)$$

with $V$ as the potential difference between two points, $R$ as the resistance and $I$ as the current. If a homogeneous sample is placed between two conducting electrodes with a certain area $A$ and a distance $d$ between them, the resistance $R$ can be expressed as

$$R = \rho \frac{d}{A} \quad (2.30)$$

where $\rho$ is the characteristic electrical resistivity of the material [28]. While the Ohm's Law is a well-known relationship, its use is limited to only describe ideal resistors. An ideal resistor follows the Ohm's Law at all current and voltage levels, has AC frequency independent values for the resistance and an AC current and voltage through the resistor which is always in phase [29]. In most of the materials, ideal conditions are not present, which is why a more sophisticated concept, the Impedance, is needed to describe resistors.

By employing IS, the dielectric properties of a material as a function of frequency $\omega$ at different temperatures $T$ can be determined. Therefore, a monochromatic and sinusoidal signal

$$V(t) = V_0 \sin(\omega t) \quad (2.31)$$

with the single frequency $\upsilon = \omega/2\pi$ is applied to a cell at a certain temperature and the responding sinusoidal steady state current

$$I(t) = I_0 \sin(\omega t + \theta) \quad (2.32)$$

with $\theta$ as the phase difference between the voltage and the current is measured. A purely resistive behavior ("ideal resistor") shows a phase difference $\theta$ equals to zero [29].

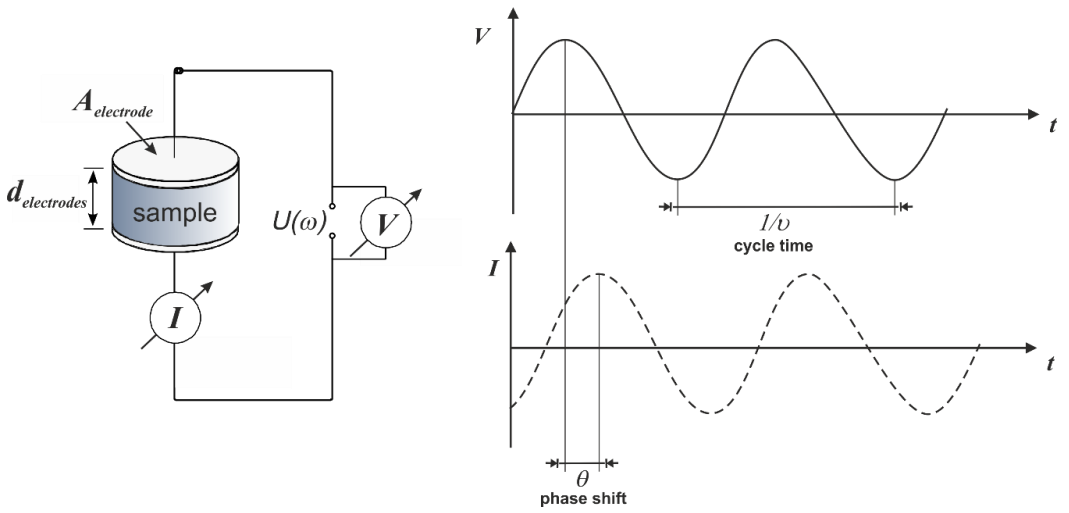


***Fig. 2.15*** Both schemes are according to [29] (l.) Schematic description of the impedance spectroscopy measurement. With the frequency dependent AC voltage V and current I , the electrode surface $A_{electrode}$ and the distance between the two electrodes around the sample $d_{electrode}$. U(ω) represents an electric AC stimulus of frequency $\nu$ (current or voltage) (r.) Schematic result of an impedance experiment with a sinusoidal input voltage V at a frequency v and its responding current I.

To calculate the complex impedance $Z(\omega, t)$ of a system analogous to Ohm's Law, the ratio of the input voltage $V(\mathrm{t})$ and the output current $I(\mathrm{t})$ are used

$$Z(\omega, t) = \frac{V(\mathrm{t})}{I(\mathrm{t})} = \frac{V_m \sin(\omega t)}{I_m \sin(\omega t + \theta)} = |Z| \frac{\sin(\omega t)}{\sin(\omega t + \theta)} \quad (2.33)$$

with $|Z|$ as its absolute value. Using the Euler's relationship

$$\exp(i\theta) = \cos(\theta) + i sin(\theta) \quad (2.34)$$

it is possible to express the impedance as a complex function.

The complex potential $\tilde{V}(\mathrm{t})$ can be described as

$$\tilde{V}(\mathrm{t}) = V_0 \exp(i\omega t) \tag{2.35}$$

and the complex current response $\tilde{I}(t)$as

$$\tilde{I}(\mathrm{t}) = I_0 \exp(i(\omega t - \theta)) \tag{2.36}$$

The impedance is now represented as a complex number which can be expressed as a combination of a real and in phase part ($Z'$) and an imaginary out of-phase-part ($Z''$) [29]:

$$\tilde{Z}(\omega, t) = \frac{\tilde{V}(\mathrm{t})}{\tilde{I}(\mathrm{t})} = \left|\tilde{Z}\right| \exp(i\theta) = \left|\tilde{Z}\right|\big(\cos(\theta) + isin(\theta)\big) = Z' + iZ'' \tag{2.37}$$

The reciprocal value of the impedance is called the admittance $\tilde{Y}(\omega, t)$ and can be written as $\tilde{Y}(\omega, t) \equiv \tilde{Z}(\omega, t)^{-1} \equiv Y' + iY''$[27].

If the impedance measurements are performed on samples between two parallel and even electrodes, the specific impedance $\tilde{\rho}$

$$\tilde{\rho} = \tilde{Z} \cdot \frac{d}{A} \tag{2.38}$$

and the specific admittance $\tilde{\sigma}$

$$\tilde{\sigma} = \frac{1}{\tilde{\rho}} = \tilde{Y} \cdot \frac{d}{A} \tag{2.39}$$

should be introduced, too. The specific admittance $\tilde{\sigma}$ can be separated again in a real and an imaginary part

$$\tilde{\sigma} = \sigma' + i\sigma'' \tag{2.40}$$

Especially the real part of the specific admittance $\sigma'$ is important, because conductivity spectra are made, by plotting $\sigma'$ versus the frequency $\nu$ [27]. Conductivity spectra will be discussed in more detail in one of the next chapters.

### 2.5.2 Capacitance, permittivity and the modulus function

If a non-conducting material is positioned between two parallel electrodes with a spacing $d$, the circuit element is called a capacitor (***Fig. 2.15***, (l.)). Capacitors can store a charge per volt on the electrode surfaces, which is referred to as capacitance [F = As/V].

In a medium, the capacitance C per unit area is expressed as

$$C = \varepsilon_0 \varepsilon_r' \frac{A}{d} \tag{2.41}$$

where $\varepsilon_0$ is the permittivity of the vacuum ($8.85435 \cdot 10^{-12} Fm^{-1}$), $\varepsilon_r'$ is the relative permittivity (defined as $\varepsilon'/\varepsilon_0$ with $\varepsilon$ as the absolute permittivity), $A$ is the area of the electrodes [30].

Dielectric analysis usually determines the permittivity and conductivity properties of a material as a combined "complex permittivity" $\bar{\varepsilon}$. The concept is analogous to the concept of the complex impedance $\bar{Z}$ which is why the complex permittivity can be expressed as a function with a real permittivity (often referred to as 'permittivity' or 'dielectric constant') $\varepsilon'$ and the imaginary permittivity (or 'loss factor') $\varepsilon''$ as:

$$\tilde{\varepsilon} = \varepsilon' + i\varepsilon'' \tag{2.42}$$

The real part $\varepsilon'$ describes the energy storage while the imaginary part $\varepsilon''$ describes the ionic conduction [27].

The inverse value of the dielectric permittivity $\tilde{\varepsilon}^{-1}$ is the modulus function $\widetilde{M}$ with

$$\widetilde{M} = M' + iM'' = i\omega C_0 \tilde{Z} \tag{2.43}$$

with $C_0 = \varepsilon_0 A/d$ as the capacitance of an empty measuring cell [27].

### 2.5.3 Data representations

The ionic conductivity (real part) and the dielectric permittivity (real part) are generally plotted against the measurement frequency in a double logarithmic graph (***Fig. 2.16***). The characteristic shapes of the resulting isotherms are used, to determine important information about the hopping characteristics of the ions in the sample [31].

***Fig. 2.16*** can be separated in three main sections. The diagram starts on the left side at low frequencies with section (I). At intermediate temperatures and going to higher frequencies, the slope of the upcoming ion conductivity ($\sigma'$) decreases while the value of the incoming permittivity ($\varepsilon'$) decreases rapidly. This phenomenon is called electrode polarization and results from the applied metallic electrodes [31]. The polarization effect is a result of a sufficiently fast ion transport, causing a pilling up of the ions at the blocking electrode surface [32]. This leads to a drop of the conduction and a large bulk polarization in the sample.

Even if the polarization effect results directly from the moving ions, it is a nonequilibrium, extrinsic feature and depends on the nature of the electrode interface as well as the thickness of the specimen.

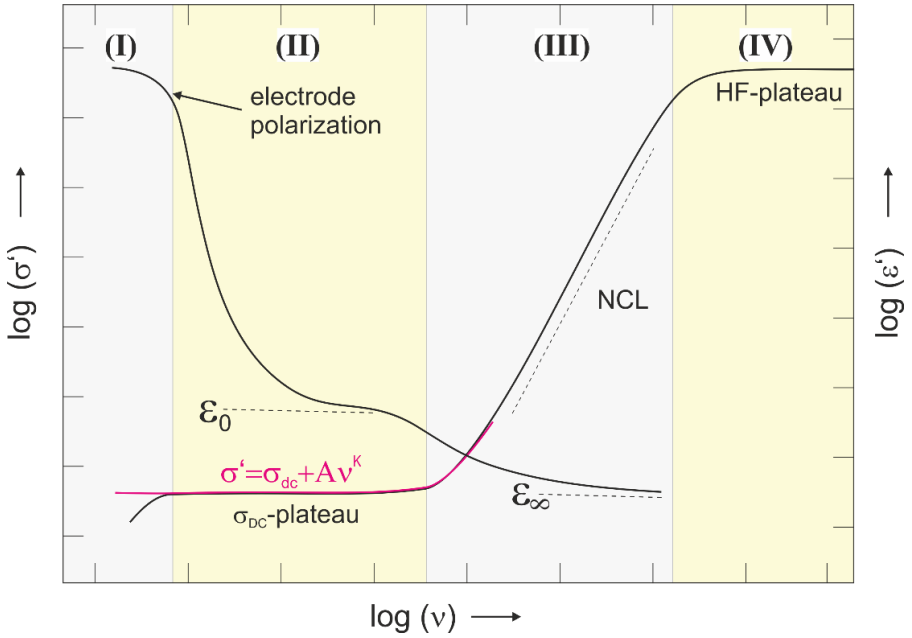


**Fig. 2.16** Typical shape of the conductivity ($\sigma'$) and permittivity ($\varepsilon'$) isotherms for solid ion conductors as a function of the frequency. Scheme according to [31].

Moving to higher frequencies (section (II)), a plateau area for the conductivity isotherm becomes visible, which is called the *DC-conductivity plateau*. The plateau values represent the long-range diffusion of ions as they hop from site to site through the matrix of the sample [31]. The diffusion is Arrhenius-activated according to $\sigma_{DC}T \propto \exp(-E_A/k_BT)$ and allows the determination of the average activation energy for a successful jump of the ions [14] expressed as

$$\sigma_{DC}T = \sigma_0 \exp\left(-\frac{E_{A,DC}}{k_BT}\right) \qquad (2.44)$$

where $\sigma_{DC}$ represents the DC-ion conductivity, $E_{A,DC}$ the activation energy for the DC-plateau and $k_B$ the Boltzmann constant.

In the dielectric isotherm, a shoulder appears which refers to the set in of a polarization in the same frequency range. The polarization is related to the growth and shrinkage of a dipole moment that occurs during the hops in the hopping process. The growth and shrinkage is in many respects similar to the rotational relaxation which occurs for a collection of noninteracting

permanent dipoles of a dipole moment *p*. The shoulder of the dielectric isotherm corresponds directly to the DC-plateau of the conductivity isotherm, which belong both to the same process.

Moving still further to higher frequencies (section (III)), a major increase of the ion conductivity as well as a leveling off in the permittivity can be seen. The conductivity shows a linear frequency-dependence which is why the region is called *nearly constant loss* (*NCL*) *regime* [31]. The NCL is still much debated, but in general it is considered to represent localized motion and is considered to be related to the relaxation behavior of unsuccessful forward-backward jumps. The decrease in the dielectric permittivity results from an elastic polarization of the atoms of the matrix [14].

Finally, there is a second plateau existing (section (IV)), a so-called high-frequency (HF) plateau, where every jump contributes to the conductivity. But in practice, the detection is difficult, because the signal of the ion conductivity gets mixed and overlapped by vibrational contributions of the conductivity [33].

The charge diffusion coefficient $D^{\sigma}$ can be determined by using the *Nernst-Einstein relation* ( 2.12), knowing the values for the ionic conductivity $\sigma_{DC}$ and the charge carrier density $N$.

It is possible to approximate the experimental impedance data by using the impedance of an equivalent circuit of ideal resistors and capacitors and arranging it in a series or a parallel connection. The impedance values for the ohmic resistance ($\tilde{Z}_R$) and the capacitance ($\tilde{Z}_C$) can be expressed as

$$\tilde{Z}_R = R \tag{2.45}$$

$$\tilde{Z}_C = \frac{1}{i\omega C} = -\frac{1}{\omega C} \tag{2.46}$$

with *R* representing the ohmic resistance and *C* the capacitance [33].

The two previous relations can be used to calculate the impedance and admittance of a *series* and a *parallel connection*. To work with the analogy of circuits, a representation known as *Cole-Cole* (or *Nyquist*) plot, can be used. It presents the impedance data in the complex impedance plane [16].

Regarding to ***Fig. 2.17***, the equivalent circuit (A') consists out of a capacitor $C_S$ and a resistor $R_S$ connected *in series*. The formula to calculate the impedance for such a series connection is defined as

$$\tilde{Z} = Z' + iZ'' = R_S - iX_S \tag{2.47}$$

containing $X_S$ , called the reactance.

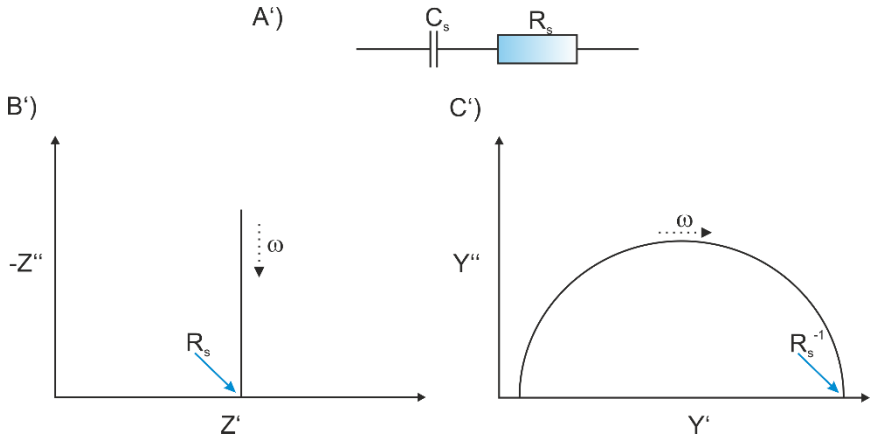


***Fig. 2.17*** (A') Equivalent circuit of the **series connection** ($_s$) of the capacitor $C_s$ and the resistor $R_s$. (B') Corresponding Cole-Cole plot for the impedance (−Z'' vs Z'). (C’) Corresponding Cole-Cole plot for the admittance (Y'' vs. Y'). For (B’) and (C’), the frequency ω increases in the direction given by the black dashed arrows. Scheme according to [34].

the reactance $X_S$ itself, is defined as

$$X_S = \frac{1}{\omega C_S} \tag{2.48}$$

To calculate the admittance, the following relation is given by

$$\tilde{Z} = \frac{R_S}{R_S^2 + X_S^2} + i\frac{X_S}{R_S^2 + X_S^2} \tag{2.49}$$

The blue arrows in the Cole-Cole plot for the impedance and admittance (***Fig. 2.17*** (B’), (C’)) mark the intercepts of the graphs with the $Z'$ and $Y'$ axis (real parts), which provide the resistance values $R_S$ [34].

Regarding to ***Fig. 2.18***, the equivalent circuit (A’’) consists out of a capacitor $C_P$ and a resistor $R_P$ connected *parallel*.

The formula to calculate the impedance for such a parallel connection is defined as

$$\tilde{Z}^{-1} \equiv \tilde{Y} \tag{2.50}$$

$$\tilde{Y} = Y' + iY'' = G_P + iB_P \tag{2.51}$$

with $G_P$ and $B_P$ as variables for the resistance

$$G_P = R_P^{-1} \tag{2.52}$$

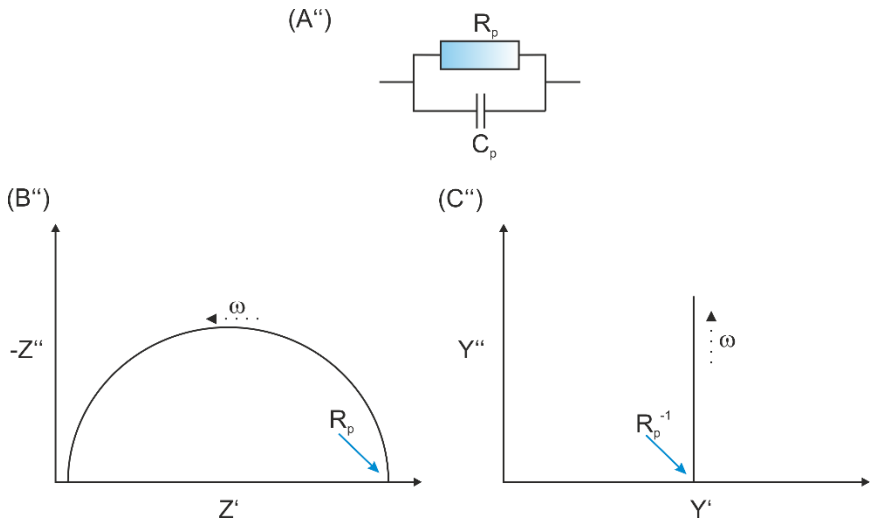


**Fig. 2.18** (A") Equivalent circuit of the **parallel connection** ($_p$) of the capacitor $C_p$ and the resistor $R_p$. (B") Corresponding Cole-Cole plot for the impedance (–Z" vs Z'). (C") Corresponding Cole-Cole plot for the admittance (Y" vs. Y'). For (B") and (C"), the frequency $\omega$ increases in the direction given by the black dashed arrows. Scheme according to [34].

and the susceptance

$$B_P = \omega C_P \tag{2.53}$$

Using these two terms, the impedance for a parallel series can be calculated as

$$\tilde{Z} = \frac{G_P}{G_P^2 + B_P^2} - i\frac{B_P}{G_P^2 + B_P^2} \tag{2.54}$$

The blue arrows in the Cole-Cole plot for the impedance and admittance (***Fig. 2.18***, (B′), (C′)) mark the intercepts of the graphs with the $Z'$ and $Y'$ axis (real parts), which provide the resistance values $R_S$ [34].

## 2.6 Nuclear magnetic resonance (NMR) spectroscopy on solids

Diffraction methods are a very good choice for the determination of static structures, but they give very little information about the dynamics in a system. Ignoring this feature of a material would mean to ignore major information on its properties. To investigate properties such as anisotropic shielding, dipole-dipole coupling between magnetic nuclear dipoles and quadrupole coupling in solids, the solid-state nuclear magnetic resonance (NMR) can be used. The investigation takes place by interfering the electronic structure of the sample and studying

the interactions in the sample. In practice, e.g. characterizing dipole-dipole coupling in samples can be helpful to measure internuclear distances [35].

### 2.6.1 The vector model for pulsed NMR

The vector model for pulsed Nuclear magnetic resonance spectroscopy is a suitable model for isolated spin-$\frac{1}{2}$ nuclei, which are not coupled to other nuclei. It also provides a convenient picture of the effects of radio frequency (rf) pulses on such a system. Nuclear magnetic resonance spectroscopy measures the net magnetization $\vec{M}$ (bulk magnetic moment) arising from the nuclei in a sample and is the vectorial sum of all single individual magnetic moments $\mu$ of the nuclei (***Fig. 2.19***)

$$\vec{M} = \sum_i \mu_i \qquad (2.55)$$

where $\mu_i$ is the magnetic moments associated with the *i*th nucleus [35].

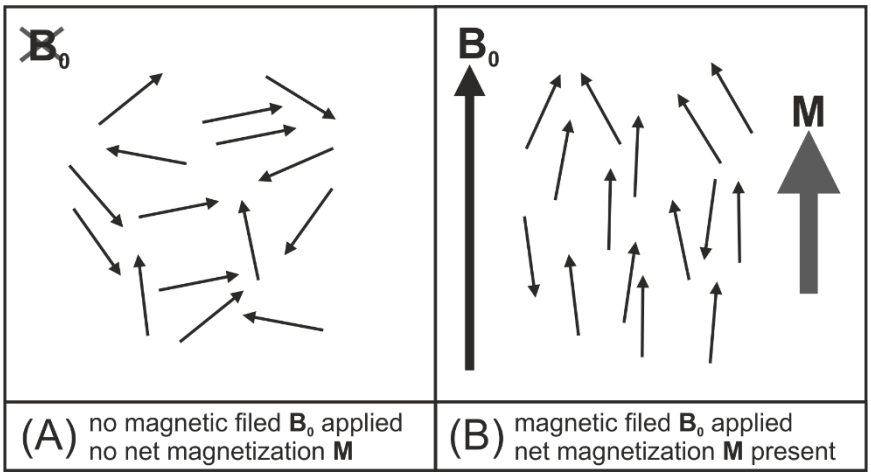


**Fig. 2.19** Schematic representation of the classical model for the formation of the net nuclear magnetization $\vec{M}$ in a sample. In the absence of a magnetic field $\vec{B}_0$, the individual nuclear magnetic moments $\mu_i$ (represented by vector arrows) have random orientations so that there is no net magnetization (A). If $\vec{B}_0$, is applied, all $\mu_i$ are aligned along the magnetic field leading to a net nuclear magnetization. Thermal effects cause a distribution of orientations rather than perfect alignment (B). Scheme according to [35].

type of nucleus $\gamma$, called the magnetogyric ratio

$$\mu_i = \gamma \vec{I}_1 \qquad (2.56)$$

Finally, the net magnetization can be written as

$$\vec{M} = \gamma \vec{J} \qquad (2.57)$$

where $\vec{J}$ is the net spin angular momentum of the sample.

If the nuclei are placed in a uniform magnetic field $\vec{B}_0$, along the z-axis (0,0, $\vec{B}_0$), a torque $\vec{T}$ is exerted on the magnetization vector:

$$\vec{T} = \frac{d}{dt}\vec{J} \qquad (2.58)$$

In turn, the torque in this situation is given by

$$\vec{T} = \vec{M} \times \vec{B}_0 \qquad (2.59)$$

Combining Equations (2.57), (2.58) and (2.59), the motion of the magnetization vector $\vec{M}$ in the magnetic field $\vec{B}_0$ can be written as

$$\frac{d\vec{M}}{dt} = \gamma[\vec{M} \times \vec{B}_0] \qquad (2.60)$$

Eq. (2.60) shows that $\vec{M}$ precesses in $\vec{B}_0$ at a constant rate

$$\omega_0 = \gamma \vec{B}_0 \qquad (2.61)$$

The frequency $\omega_0$ is called the *Larmor frequency* which shows characteristic values for each nucleus [35, 36]. At a thermal equilibrium, the magnetic moments precess in the magnetic field $\vec{B}_0$ around the z-axis with $\vec{M}_z = \vec{M}_0$ and $\vec{M}_x = \vec{M}_y = 0$ [37].

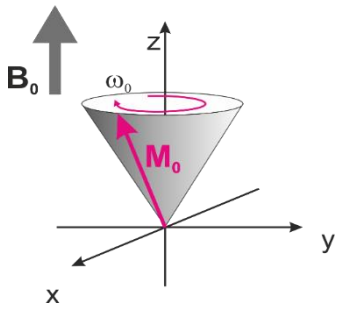


**Fig. 2.20** Precession of the magnetization $\vec{M}_0$ in an external magnetic field $\vec{B}_0$ in a thermal equilibrium, according to [14].

The simplest spin system consists of an isolated spin in the static, uniform magnetic field of the NMR with no other interactions present. The Hamiltonian $\hat{H}$ for a nuclear spin in a static field is

$$\hat{H} = -\vec{\hat{\mu}} \cdot \vec{B}_0 \qquad (2.62)$$

where $\vec{\hat{\mu}}$ is the nuclear magnetic moment operator.

This Hamiltonian is often referred to as the *Zeeman Hamiltonian*. $\vec{\hat{\mu}}$ can be written in terms of the nuclear spin operator $\hat{I}$:

$$\vec{\hat{\mu}} = \gamma\hbar\vec{\hat{I}} \qquad (2.63)$$

By combining Eq. (2.62) and (2.63) and applying the magnetic field along the z-direction, the following relation can be obtained

$$\hat{H} = -\gamma\hbar\hat{I}_z\vec{B}_0 \qquad (2.64)$$

For a spin with $I = \frac{1}{2}$ and $m = \pm\frac{1}{2}$, there are two possible eigenstates with two energy levels $E_{\frac{1}{2},\pm\frac{1}{2}} = \mp\frac{1}{2}\gamma\hbar\vec{B}_0$ **(*Fig. 2.21*)**. These states are frequently referred to as *Zeeman states*. The transition energy $\Delta E$ between the two spin states is $\gamma\hbar\vec{B}_0$Converted in frequency units, this corresponds to $\Delta E = \gamma\hbar\vec{B}_0 = \hbar\omega_0 = h\nu$ [35, 36].

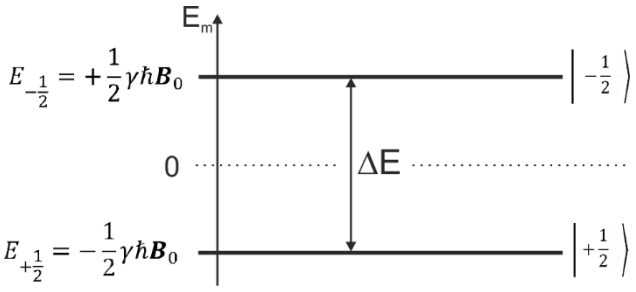


**Fig. 2.21** Energy levels for a spin-$\frac{1}{2}$ nucleus in a magnetic field $\vec{B}_0$. The levels are labelled according to their magnetic quantum number *m* according to [35].

### 2.6.2 The effects of Radio Frequency Pulses in NMR

To carry out pulsed NMR experiments, radio frequency (rf) fields $\vec{B}_{rf}$ are used to interfere the thermal spin equilibrium of a sample. A rf-coil generates the field along the tilted axis shown in ***Fig. 2.22***. During an rf-pulse on a single spectrometer channel, the magnitude of the field oscillates at a spectrometer reference frequency $\omega_{rf}$. Between pulses, the rf-field is equal to zero.

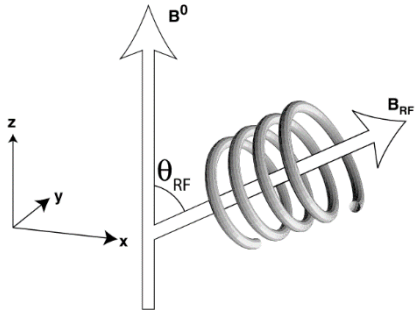


**Fig. 2.23** The rf-coil and the applied fields $\vec{B}_0$ and $\vec{B}_{rf}$. The scheme was taken from [37].

If the pulse is perpendicular to the magnetic field $\vec{B}_0$ then the rf field has the form (***Fig. 2.24***)

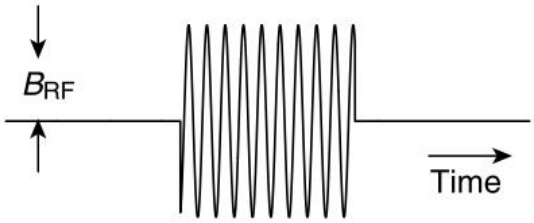


**Fig. 2.24** An oscillating rf field. The scheme was taken from [37].

The rf field corresponds to the following mathematical relation. During an rf pulse, it can be described as

$$\vec{B}_{rf}(t) = B_{rf}\left(e_z cos\theta_{rf} + e_x sin\theta_{rf}\right)\cos(\omega_{rf}t + \Phi_p) \qquad (2.65)$$

otherwise as

$$\vec{B}_{rf}(t) = 0 \qquad (2.66)$$

where $B_{rf}$ is the maximum rf amplitude during the pulse and $e_x$ and $e_y$ are the unit vectors in the coordinate system.

The rf field consist of a longitudinal component proportional to $cos\theta_{rf}$ plus a transverse component proportional to $sin\theta_{rf}$. It can be useful to imagine the transverse oscillating field as the sum of two rotating components in the x,y-plane, both rotating at the same frequency but in opposite directions. The transverse component rotating in the same direction as the spin precession is called the *resonant* component of the rf field and the transverse component rotating in the opposite sense to the Larmor frequency is called *non-resonant* rf field component [37].

### 2.6.3 Spin relaxation rates

Immediately after the irradiation of the rf-pulse, the relaxation of the magnetization towards the thermal equilibrium takes place. The relaxation is characterized by two time constants $T_1$ and $T_2$. $T_1$ represents the *longitudinal* (or. *spin-lattice*) *relaxation time* and $T_2$ stands for the *transversal* (or *spin-spin*) *relaxation time.*

The change of the magnetization $\vec{M}$**,** which is a function of $T_1$ and $T_2$, can be described by

$$\frac{d\vec{M}_{z=z'}}{dt} = \frac{\vec{M}_0 - \vec{M}_{z=z'}}{T_1} \quad (2.67)$$

$$\frac{d\vec{M}_{x'}}{dt} = -\frac{\vec{M}_{x'}}{T_2} \quad (2.68)$$

$$\frac{d\vec{M}_{y'}}{dt} = -\frac{\vec{M}_{y'}}{T_2} \quad (2.69)$$

The spin-spin relaxation time $T_2$ represents the relaxation of the magnetization $\vec{M}$ in the x',y'-plane. $T_2$ is associated to exchange processes in the spin-spin system. The systems energy remains constant, but the entropy increases. The relaxation process is induced by inhomogeneity in the magnetic field as well as by the local environments of other nuclei. Especially the latter effect allows structural investigations by employing NMR. In addition, diffusion and motion processes of ions in the local polar fields of the nuclei contribute to the transversal relaxation rate, too. [14, 38, 39]

By measuring the decay of the magnetization along the y'-direction as a function of time, $T_2^*$ can be calculated via

$$\vec{M}_{y'}(t) = \vec{M}_0 \exp(-\frac{t}{T_2^*}) \quad (2.70)$$

The new notation $T_2^*$ shall indicate, that the above-mentioned relaxation processes contribute to it. The decay of the magnetization $\vec{M}$ induces an alternating potential in the rf-coil, which is positioned in the x,y-plane of the magnetic field:

$$U(t) = U_0 \exp(-\frac{t}{T_2^*}) \quad (2.71)$$

$U(t)$ is the resulting signal and is referred to as the *free induction decay* (FID). With a Fourier-Transformation (FT), the time-dependent signal is converted to a frequency dependent signal, yielding a Lorentz-shaped function [14]

$$U(\omega) = \frac{1}{2\pi} \int_{+\infty}^{-\infty} U(t) \exp(-i\omega t)\, d\omega \quad (2.72)$$

$_0$

$T_1$, the spin-relaxation time, is the time in which the spin system transfers the absorbed energy from the rf-pulse to the lattice by a depopulation of Zeeman levels with a higher energy. This results in the buildup of a magnetization along the z-axis ($\vec{M}_z = \vec{M}_0$). The motion of the ions in the sample cause fluctuations in the field of the nuclei which induce the relaxation [14, 38, 39]. Relation (2.73) describes the magnetization as a function of time

$$\vec{M}_z(t) = \vec{M}_0 (1 - \exp\left(-\frac{t}{T_1^*}\right)) \quad (2.73)$$

# 3 Experimental

## 3.1 Synthesis of $BaLiF_3$

### 3.1.1 Synthesis of $BaLiF_3$ (HK1 and HK2)

$BaLiF_3$ was prepared by high-energy ball milling of an equimolar mixture of $BaF_2$ (Chempur, 99.9 %) and LiF (Sigma-Aldrich, 99.98 %, metal basis) using a Fritsch Pulverisette 7 (premium line). Two 45 mL grinding beakers ($ZrO_2$) with 180 balls each ($ZrO_2$, 5 mm in diameter) were used. The beakers were filled under argon atmosphere to prevent contamination by moisture and oxygen during the milling process. The mixture (total mass of 10.063 g) was first milled for $t_{milling}$ = 180 min with 600 rpm under argon atmosphere, consisting of 12 cycles (HK1). Most of the obtained material (9.80 g) was further milled a second time ($t_{milling}$ = 420 min) with 600 rpm under argon atmosphere, consisting of 28 cycles (HK2). Every cycle was divided into 15 min of milling and 15 min of resting time to prevent overheating. The compositions of the milled mixture can be found in the appendix (see ***Table I***). The synthesis was modified but performed according to the procedure from [12].

### 3.1.2 Synthesis of $BaLiF_3$ (HK3)

A second $BaLiF_3$ sample was also prepared by high-energy ball milling of an equimolar mixture of $BaF_2$ (Chempur, 99.9 %) and LiF (Sigma-Aldrich, 99.98 %, metal basis) using a Fritsch Pulverisette 7 (premium line). Two 45 mL grinding beakers ($ZrO_2$) with 140 balls each (ZrO2, 5 mm in diameter) were used. Analogous to 3.1.1, the mixture (total mass of 2.000 g) was milled for $t_{milling}$ = 180 min with 600 rpm under argon atmosphere, consisting of 12 cycles (HK3). The compositions of the milled mixture can be found in the appendix (see ***Table II***). The synthesis was performed according to the procedure from [12].

## 3.2 Tempering of HK2 and HK3 to HK4 and HK5

In order to obtain tempered samples, HK2 (500 mg) and HK3 (500 mg) were weighted in ceramic dishes ($Al_2O_3$) under argon atmosphere. The samples were then tempered for 24 h at 600 °C in a tube furnace in a constant argon flow. The resulting samples named HK4 (tempered

HK2) and HK5 (tempered HK3) were stored under argon atmosphere in a glovebox. The synthesis was performed according to the procedure from [12].

## 3.3 Characterization of the $BaLiF_3$ samples

The obtained powders were characterized by X-ray powder diffraction (XRPD), using a Bruker D8 Advance diffractometer with a Bragg Brentano geometry (Cu-$K_\alpha$ radiation).

A Novocontrol Concept 80 broadband dielectric spectrometer was employed to record impedance data between 0.01 Hz to 10 MHz and 173.15 K to 473.15 K and 573.15 K respectively. To measure the samples HK2, HK3, HK4 and HK5, cylindrical pellets with a diameter of 5 mm and a thickness of approximately 1 mm were pressed under argon atmosphere, by applying an uniaxial pressure of 0.5 t. The detailed parameters can be found in the appendix (see ***Table III***). Gold electrodes of 100 nm were sputtered on both sides of the samples at 40 mA, employing a Leica EM SCD 050 evaporator.

Static $^{7}Li$ and $^{19}F$ NMR spectra for a temperature range of 253 K to 543 K were acquired with an Avance III solid-state NMR spectrometer (300 MHz). For the measurements, the samples were enclosed in a glass capillaries under vacuum conditions.

# 4 Results and discussion

## 4.1 Characterization by X-ray diffraction spectroscopy

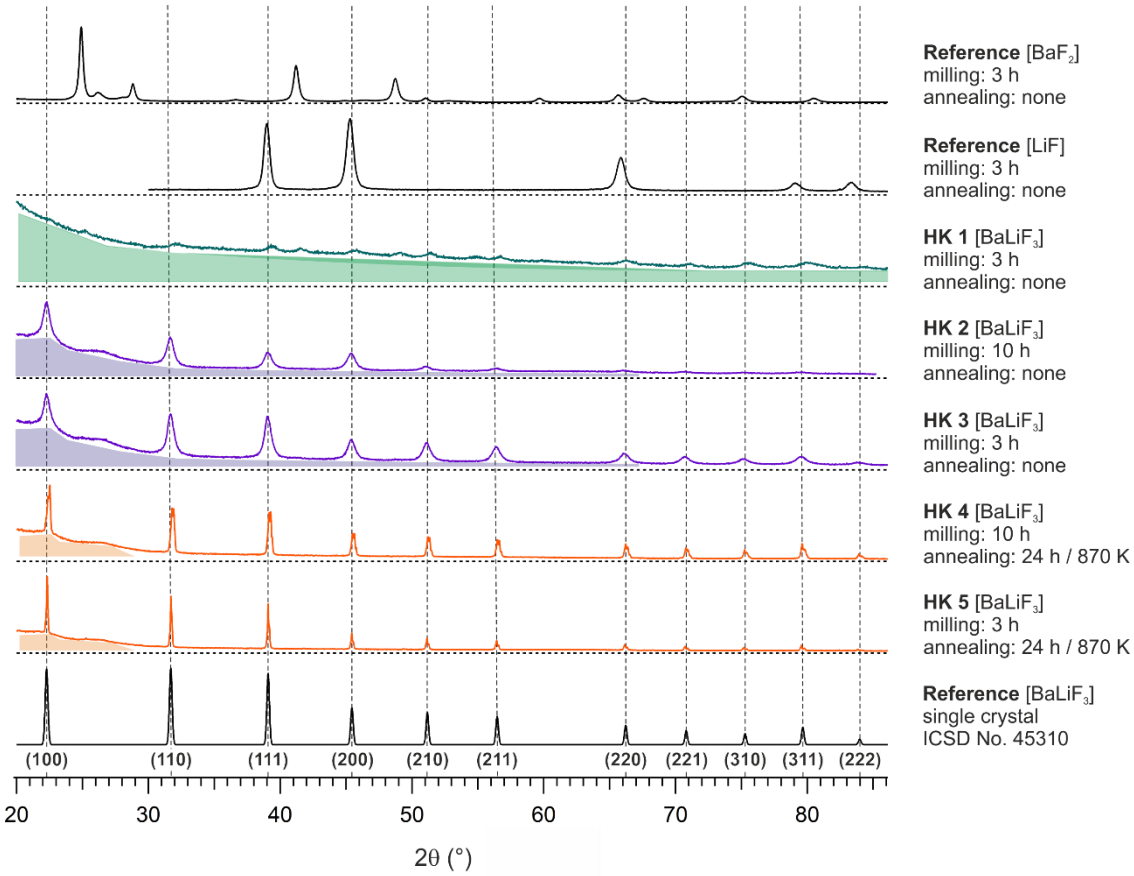


**Fig. 4.1** X-ray powder diffraction (XRPD) pattern of the various synthesized inverse perovskite $BaLiF_3$ samples (HK1 to HK5) as well as the reference XRPD pattern for the educts ($BaF_2$, LiF) and the product ($BaLiF_3$). The dashed lines shall point out the positions of the reflections of the educts $BaF_2$ and LiF. The filled-out areas below the patterns for HK1 to HK5 point out the amorphous regions of the samples.

***Fig. 4.1*** shows the X-ray powder diffraction (XRPD) pattern of the various synthesized $BaLiF_3$ samples HK1, HK2, HK3, HK4 and HK5. Reference XRPD pattern for the educts ($BaF_2$, LiF) and the product ($BaLiF_3$) are also illustrated. The data for the XRPD of the educts were obtained from previous measurements by S. Breuer. The data for the XRPD of the product were taken from the ICSD database of the FIZ Karlsruhe.

Starting with the diffractogram of sample HK1 (green), which was obtained by milling the stoichiometric mixture of the educts for 3 h (according to [12]), one can see, that its shape differs most from the other samples HK2 to HK5. Comparing the result with the clearly defined and narrow reflections of the $BaLiF_3$ reference (single crystal), the first thing coming up is the huge ‘background signal’ (indicated by the shaded areas under the reflection lines). The ‘background signal’, or better referred to as signal broadening, indicating a significant amount

of amorphous material in the sample. Such samples only show a statistical preference for interatomic distances, which is why the result of an X-ray scattering experiment will be a curve with a little number of broad maxima [24]. Sample HK1 is not completely amorphous, but it has a much smaller degree of crystallinity, compared to the single crystal reference. Moreover, not all the educts were converted into $BaLiF_3$, since there are some reflections originating from the educts $BaF_2$ and LiF, clearly visible for example at 39.0 $°2\theta$ and 45.3 $°2\theta$. The cause for this effect might be the low ball-to-powder ratio (*BP-ratio*) of 360 balls to 10.063 g powder used for the synthesis. Usually, approximately 4 g of a substance are used for the same amount of milling balls. The lower the BP-ratio, the smaller is the specific energy input into the sample [11]. The effect of the mechanochemically treatment seems to change with the BP-ratio, yielding various products. The XRPD pattern of HK1 indicate, that the formation of crystalline $BaLiF_3$ from the crystalline educts $BaF_2$ and LiF takes place by forming an amorphous intermediate phase.

In an attempt to increase the crystallinity of HK1, the sample was further milled for 7 h yielding sample HK2 (total milling time 10 h) (**Fig. 4.1**). To compare the properties, a second $BaLiF_3$ sample called HK3 was synthesized. The diffractograms of both samples show reflections at angles in accordance with the $BaLiF_3$ reference from the ICSD database. Nevertheless, some amorphous fractions in both samples are still present between 20 $°2\theta$ and 50 $°2\theta$. It is also obvious, that the reflections of HK2 and HK3 are broadened compared to those of the single crystal reference, which can have two main reasons. Theoretically, diffraction on a single crystal should show reflections without any width (*Dirac delta functions*), but in real measurements, line broadening can be present due to instrument effects or the structure of the specimen. The influence of the X-ray diffractometer depends on the wave length distribution and anomalies, but with regularly serviced instruments, the effect should be negligible. Therefore, the line broadening will mainly originate from a second quantity, the microstructural parameters and lattice imperfections in the specimen, such as dislocations, vacancies, interstitials and lattice strain. If a crystal is cracked and milled into smaller domains, stacking faults, twins and other imperfections, they also contribute to a line broadening [40]. With smaller crystallites, less lattice layers are present for each particle. As a result, less interference of the X-ray radiation with the single crystallite domains takes place, which leads to broader reflections.

Taking a look at Scherrer's equation

$$D_{hkl} = \frac{K \cdot \lambda \cdot 360°}{2\pi \cdot FWHM_{hkl}[°2\theta] \cdot cos\theta} \quad (4.1)$$

with the crystallite size $D_{hkl}$, $K$ as the Scherrer factor, $\lambda$ as the applied wave length, $2\pi \cdot FWHM_{hkl}[°2\theta]$ as the full width at half maximum (FWHM) for a reflection (*hkl*) in [°2$\theta$] and $\theta$ as the diffraction angle in [°], helps for a better understanding [12]. The line broadening of HK2 and HK3 compared to the $BaLiF_3$ reference, is thus the result of a decreasing particle size as well as introducing stress via mechanochemical treatment to the system.

In step two, HK2 and HK3 were tempered for 24 h at 870 K according to [41], yielding HK4 (previously HK2) and HK5 (previously HK3). The heat treatment led to much narrower reflections compared to the non-heat-treated samples (s. ***Fig. 4.1***). Keeping a mechanochemically treated sample for several hours at elevated temperatures, leads to an increased ion motion and promotes the rearrangement of the ions and atoms in the disordered lattice. This can lead to a reduction of defects, also known as *healing*. Heating up the samples for a couple of hours promoted the growth of larger crystallite domains [40, 42], but did not result in a phase change of the $BaLiF_3$ sample.

The crystallite sizes of the samples (***Table 1***), were calculated using Scherrer's equation ( 4.1) with $K$ = 0.94 and $\lambda_{K,\alpha}$ = 0.154 nm. The lattice parameter $a$ of the cubic system was determined by using formula

$$a = \frac{\lambda\sqrt{h^2 + k^2 + l^2}}{2\sin(\theta)} \quad (4.2)$$

which results from merging formulas ( 2.23) and ( 2.24). $\lambda$ denotes the applied wave length and $h, k, l$ the Miller indices for a reflection maximum at a diffraction angle °2$\theta$.

**Table 1** Crystallite size $D_{hkl}$ and lattice parameter a of the samples HK1 to HK5. The $D_{hkl}$ values were calculated using Scherrer's equation ( 4.1). *a* was calculated using formula ( 4.2).

| Sample | $\boldsymbol{D_{hkl}}$ (nm) | *a* (Å) |
|---|---|---|
| **HK1** | - / amorphous fractions | - |
| **HK2** | 15 | 3.99 |
| **HK3** | 15 | 3.99 |
| **HK4** | 41 | 3.99 |
| **HK5** | 59 | 3.99 |
| **$BaLiF_3$-reference, highly crystalline** [43] | - | 3.99 |

HK2 (15 nm) and HK3 (15 nm) have the same average crystallite size ($D_{hkl}$) after the milling process. These estimations agree with investigations by *Düvel et al.* [41]. The crystallite size of the subsequently annealed samples HK4 (41 nm) and HK5 (59 nm) increased by factor 2.7 and respectively by factor 3.9. The mean crystallite size of HK5 compared to HK4 is 1.4 times larger. The magnitude of the crystallite size for the tempered and almost identical $BaLiF_3$ sample determined via TEM micrographs by *Düvel et al.* [41], is located in the order of micrometers. The µm-scale does not match with nm-scale for the crystallites, determined by XRD measurements in this work. Due to its high percentage of amorphous fractions, no crystallite size for HK1 could be determined at all.

Taking a closer look on ***Fig. 4.2*** reveals, that the reflection pattern for HK4 and HK5 show multiple reflections for the same position.

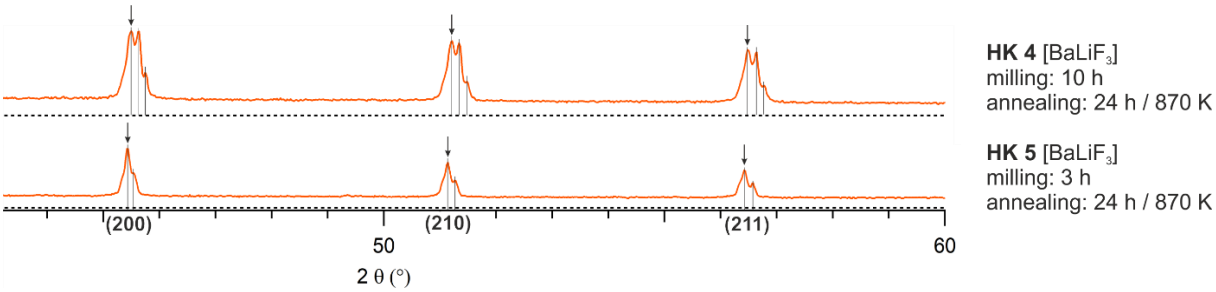


**Fig. 4.2** Close-up view from **Fig. 4.1** of the diffraction measurement of HK4 and HK5 between 44 °2$\theta$ and 60 °2$\theta$.

The doublets in HK5 could be caused by a simultaneous interference with Cu-K$_\alpha$ and Cu-K$\beta$ radiation of the X-ray source with the same (hkl)-lattice layers. If the radiation is not completely monochromatic, two reflections for the same layer could appear next to each other. The triplets in HK4 might actually be doublets with an additional shoulder towards higher angles. The shoulders in an XRPD will be probably caused by structural changes in the crystallites during the annealing process. The close-up view (***Fig. 4.2***) additionally reveals a small shift of the HK4 reflections to higher angles, compared to the reference. Both phenomena could be rooted in the varying milling procedures of HK2 and HK3. Different starting conditions at the heat-treatment can lead to a divergent stoichiometry range in the crystallite domains. Under these conditions, the crystal growth could lead to different lattice conditions, influencing the diffraction pattern. For the determination of the Bragg angles for HK4 and HK5, always the left reflection was analyzed. It has the highest intensity and is indicated by the black arrows in ***Fig. 4.2***. Concluding the above data, the annealing process led to a further reduction of the amorphous fractions for HK4 and HK5 (20 °2$\theta$ to 30 °2$\theta$, ***Fig. 4.1***).

## 4.2 Investigations on $BaLiF_3$ samples via impedance spectroscopy

The electrical behavior of HK2, HK3, HK4 and HK5 was characterized by impedance spectroscopy (IS). The name of a pallet consists of two parts. For each sample, several pallet s were produced and the ones with the most homogeneous surfaces properties were chosen for the IS (see annex, ***Table III***).

During the IS measurement, each sample went through a temperature profile, according to ***Fig. 4.3***. For each temperature, real and imaginary parts of quantities such as the conductivity, the impedance and the permittivity, were recorded in a frequency range between 0.01 Hz to 10 MHz. In compartment (**I**), the temperature of the sample was first heated up to 100 °C by leading temperature-controlled $N_2$ through the measuring chamber. The temperature was kept there for a second time interval, to bake out possibly present $H_2O$, which could falsify the IS measurement. Afterwards, the temperature was reduced step by step to −100 °C. The data obtained from compartment (**I**) will be ignored for the evaluation and was only important for preparing the pallet for the relevant section (**II**). Here, the IS measurement was performed in a temperature range between −100 °C and 200 °C with an increment of 20 °C. Compartment (**III**) was also ignored for the evaluation, and had the purpose of cooling down the specimen to room temperature.

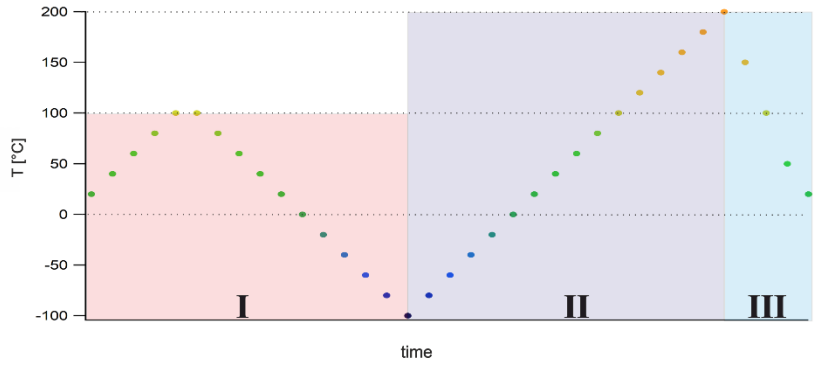


**Fig. 4.3** Temperature profile of the heating treatment during the IS.

Below in ***Fig. 4.4***, the obtained real parts of the conductivity $\sigma'$ and the applied frequencies $\nu$ from the IS experiment for sample HK2_2 (compartment (**II**)), were plotted exemplary in a double logarithmic graph. On the left side, each isotherm is labeled with the temperature, at which it was recorded.

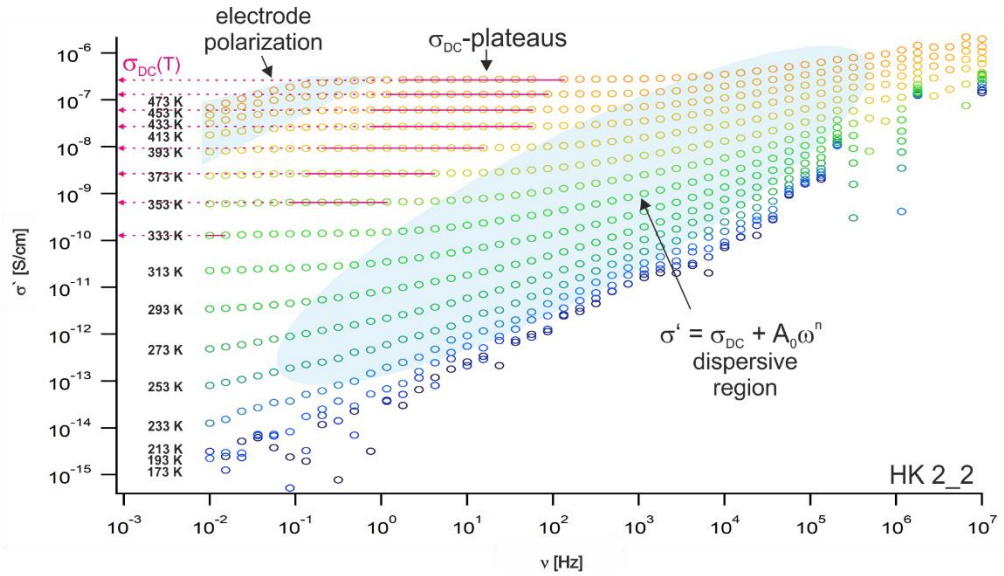


**Fig. 4.4** Conductivity plot of sample HK2_2 from the impedance measurement. The logarithmic real part of the conductivity $\sigma'$ is plotted against the logarithmic frequency $\nu$ [Hz]. The red lines denote the $\sigma_{DC}$ plateau values and the arrows extending the plateau lines mark the ion conductivity of each isotherm on the y-axis. The blue areas mark the electrode polarization and the dispersive region. The conductivity plot for HK3_1 can be found in the annex (**Fig. A**).

Looking towards lower frequencies, electrode polarization effects are present at the isotherms for the highest recorded temperatures (blue colored wedge). At low temperatures, no usable data points are available in the recorded frequency range, but with an increasing temperature, red-labeled frequency independent $\sigma_{DC}$-conductivity plateaus appear. With an increasing temperature, the plateaus shift towards higher frequencies. Going to higher frequencies (dispersive region, blue colored ellipse), frequency dependent conductivities $\sigma'$ for most of the isotherms, can be described with the Jonscher power law

$$\sigma' = \sigma_{DC} + A_0\omega^n \qquad (4.3)$$

$A_0$ is called the dispersion parameter, $\omega$ the frequency and $n$ the power law exponent [44]. The conductivity spectra of HK3_1, HK4_1 and HK5_3 were plotted the same way as illustrated in ***Fig. 4.4***. Due to the fact, that the DC-plateaus of HK4_1 and HK5_were out of the range of our measuring device (***Fig. 4.5***), the experiment was adjusted. Since the frequency range of the IS could not be further increased, but DC-plateaus can be shifted to higher frequencies at higher temperatures, the temperature range of the experiment was increased to −100 °C to 300 °C.

Two new pallets (HK4_3, HK5_4) were recorded under the new conditions, yielding a number of $\sigma_{DC}$ plateau values. ***Fig. 4.6*** exemplarily illustrates the improvements for sample HK4_3 compared to sample HK4_1 in ***Fig. 4.5***.

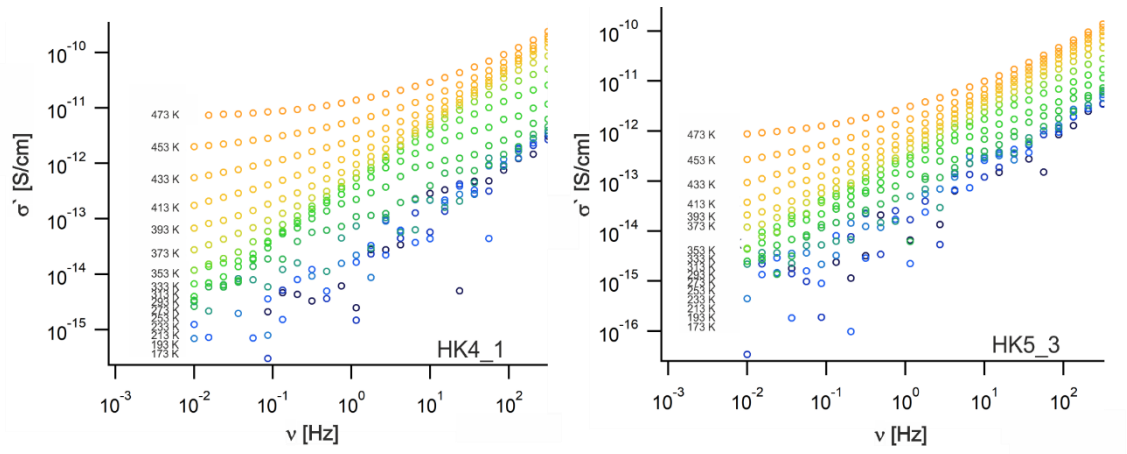


**Fig. 4.5** Conductivity plots of sample HK4_1 and HK5_3 from the impedance measurement. The logarithmic real part of the conductivity $\sigma'$ is plotted against the logarithmic frequency $\nu$. The applied temperature range of 100 °C (173.15 K) to 200 °C (473.15 K) was too small to obtain sufficient data points for the samples in the detectable frequency range of the IS.

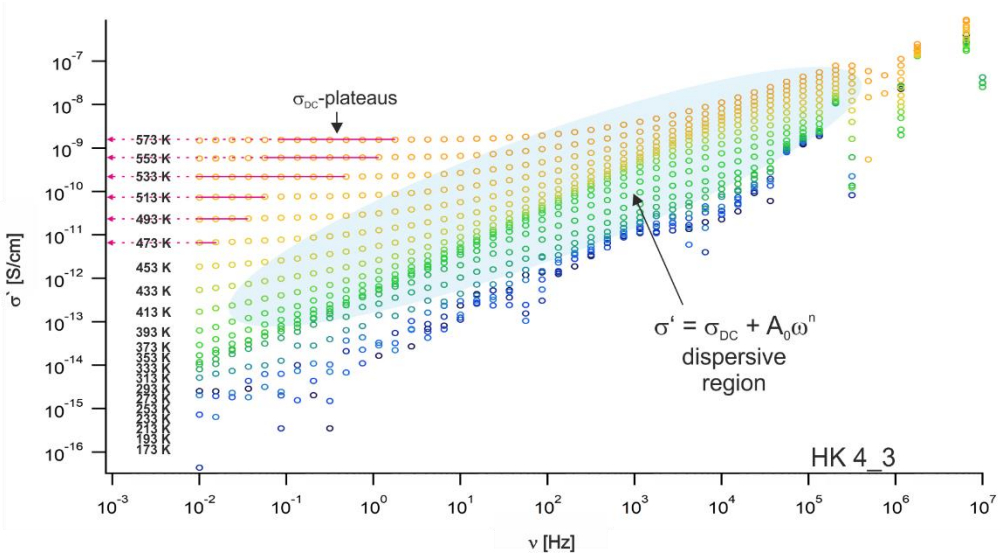


**Fig. 4.6** Conductivity plot of sample HK4_3 from the impedance measurement. The logarithmic frequency $\nu$ is plotted against the logarithmic real part of the conductivity $\sigma'$. The temperature range of 100 °C (173.15 K) to 300 °C (573.15 K) was large enough, to obtain a usable amount of $\sigma_{DC}$ plateau value. The red lines denote the $\sigma_{DC}$ plateau values and the arrows extending the plateau lines mark the ion conductivity of each isotherm on the y-axis. The blue area marks the dispersive region. The conductivity plot for HK5_4 can be found in the annex (**Fig. B**).

To quantify the thermal activation of long-range ion transports, the *DC*-conductivity values ($\sigma_{DC}\,T$) were plotted as log($\sigma_{DC}\,T$)[S K cm$^{-1}$] versus 1000/T [K$^{-1}$] in an Arrhenius-plot (***Fig. 4.7***). The lines between the data points are linear fits, which follow the Arrhenius type relation

$$\sigma_{DC}T \propto \exp(\frac{-E_A}{k_B T}) \qquad (4.4)$$

with $E_A$ representing the activation energy for ionic conduction and $k_B$ the Boltzmann constant [45, 46].

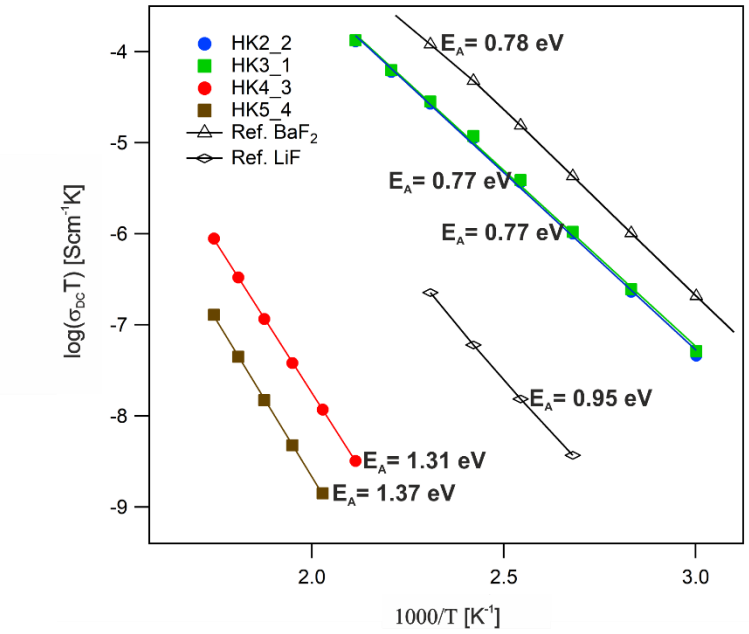


**Fig. 4.7** Arrhenius plots for the samples HK2_2 to HK5_4 with the respective activation energies $E_A$. In addition, the DC-conductivities of the educts $BaF_2$ ($t_{milling}$=10 h) and LiF ($t_{milling}$=15 h) were plotted as a reference. The data for the references was measured by *S. Breuer*.

To calculate the activation energies $E_A$, ( 4.4) can be also expressed as

$$\sigma_{DC}T = \sigma_0 \exp\left(\frac{-E_A}{k_B T}\right) \qquad (4.5)$$

By applying the natural logarithm on formula ( 4.5), a linearized Arrhenius relation

$$\ln \sigma_{DC}T = \ln \sigma_0 - \frac{E_A}{k_B T} \qquad (4.6)$$

is be obtained.

Since the natural logarithm can be transformed into the decadic logarithm according to

$$\ln(x) = 2.3 \cdot log_{10}(x) \qquad (4.7)$$

formula ( 4.6) can be written as

$$2.3 \cdot \log(\sigma_{DC}T) = 2.3 \cdot (\log \sigma_0) - \frac{E_A}{k_B T} \qquad (4.8)$$

Dividing ( 4.8) by 2.3 and converting $\frac{E_A}{k_B T}$ into $(\frac{E_A}{k_B \cdot 1000} \cdot \frac{1000}{T})$ leads to

$$\log(\sigma_{DC} T) = \left(\frac{-E_A}{1000 \cdot k_B \cdot 2.3} \cdot \frac{1000}{T}\right) + \log(\sigma_0) \qquad (4.9)$$

The mathematical conversions result in a linearized version of the Arrhenius relation, according to the general straight-line equation

$$y = m \cdot x + c \qquad (4.10)$$

**Table 2** Conversion table for the linearized Arrhenius equation.

| Section of the straight-line equation | variable | Corresponding section of the linearized Arrhenius equation ( 4.9) |
|---|---|---|
| **y-value** | y | $\log(\sigma_{DC} T)$ |
| **slope** | m | $\frac{-E_A}{1000 \cdot k_B \cdot 2.3}$ |
| **x-value** | x | $\frac{1000}{T}$ |
| **y-intercept** | c | $\log(\sigma_0)$ |

By determining the slope of each linear fit, the activation energies can be calculated with

$$E_A = -m \cdot 1000 \cdot k_B \cdot 2.3 \qquad (4.11)$$

The activation energy is a measure to specify the mean energy, ions need to perform a successful jump from one lattice site to another. The lower the activation energy, the higher is the ionic conductivity of a sample.

Even though the milling times of HK2 (0.77 eV) and HK3 (0.77 eV) differ by 7 h, the calculated activation energies $E_A$ are identical (***Fig. 4.7***). The values of 0.77 eV match with the data of other investigations (0.74(1) eV) [12]. The $BaF_2$ reference, which was milled for 10 h, has a higher activation energy of 0.78 eV, but the ion conductivity is surprisingly higher compared to the joint *anti*-perovskite $BaLiF_3$ samples HK2 and HK3. The LiF reference, which was milled for 15 h, has an even higher activation energy (0.95 eV) than $BaF_2$, but its ion conductivity a much lower. The activation energies of HK4 (1.31 eV) and HK5 (1.37 eV) differ by one order of magnitude, even if they were heat-treated under the same conditions. This could be the result of the different mechanochemically treatments, inducing different levels of

imperfections and crystallite states in the samples and influencing the subsequently annealing process. The tempered samples have higher activation energies than HK2_2, HK3_1, $BaF_2$ and LiF. Moreover, HK4_3 and HK5_4 show ionic conductivities of a magnitude 4 to 5 times lower than the non-tempered samples, which is even lower than the ionic conductivity of pure LiF.

The obtained activation energies for the tempered samples HK4 and HK5 show a much higher activation energy, compared to a similar processed $BaLiF_3$ sample by *Düvel et al.* [41] ($E_A = 1.04$ eV). A reason could be, that the samples from this work were constantly kept under an argon atmosphere, while *Düvel et al.* prepared their sample in air. Possibly, moisture in the sample, or Li in $BaLiF_3$ reacting with $O_2$ or $H_2O$ present in the air, could have altered the conductivity properties.

Another approach to investigate the electric properties of a sample is using Cole-Cole diagrams. Plotting the negative imaginary part of the impedance ($-Z''$) against the positive real part of the impedance ($Z'$) yields semicircle-shaped graphs, representing the contributions to the electrical properties associated to, e.g., bulk material, grain boundary effects and interfacial polarization phenomena [47].

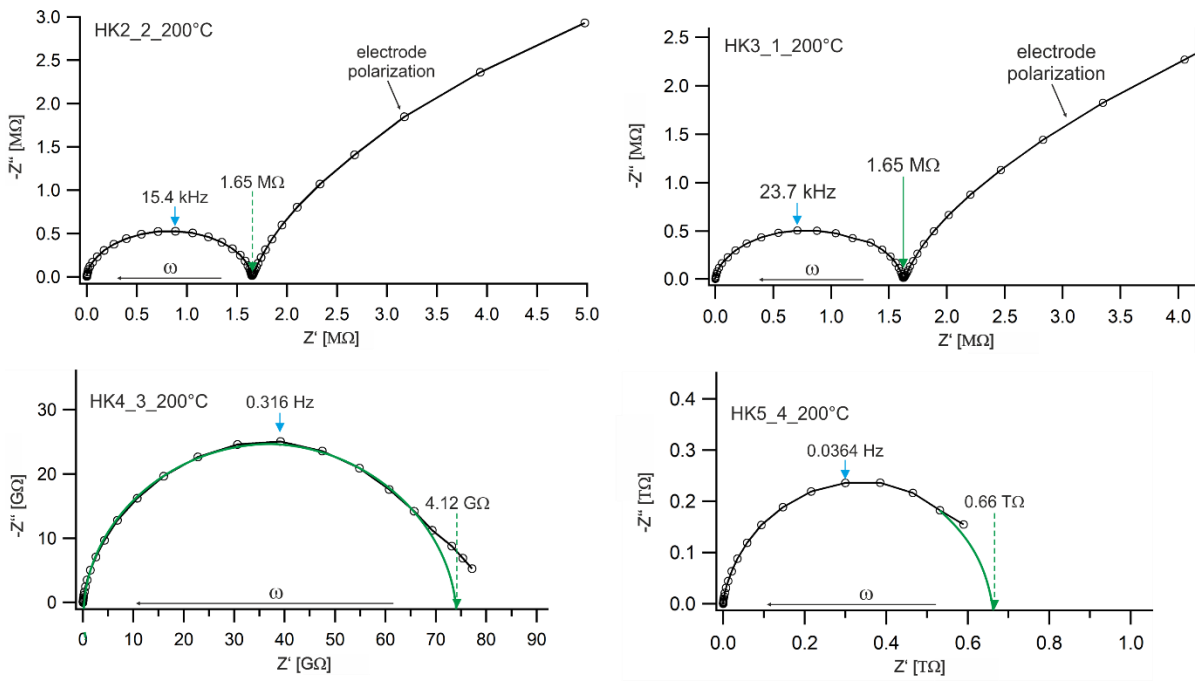


**Fig. 4.8** Cole-Cole-diagrams for all $BaLiF_3$ samples HK2_2 to HK5_4 recorded at 200 °C. The blue arrows point out the corresponding frequency $\nu$ at the maximum of the semicircle. The green dashed arrows indicate the intercept with the real part of the impedance ($Z'$). The black arrows indicate the direction, in which the frequency $\omega$ increases. Towards smaller frequencies $\omega$, an electrode polarization for HK2_2 and HK3_1 is present [54].

The calculation of the conductivity values $\sigma_{DC}$ from the Cole-Cole plot above can be done by employing equation

$$\sigma' = \frac{1}{Z'} \cdot \frac{l}{A} \quad (4.12)$$

$\sigma'$ represents the conductivity, $Z'$ the real part of the impedance, $A$ the area of the pallet surface and $l$ its thickness [48]. Assuming, that no electronic transport takes place in the material, the ionic conductivity is defined by the interception of the semicircle with the real part of the impedance ($Z'$) [34]. In ***Fig. 4.8***, this is indicated by the green dashed arrows.

Using the determined $Z'$-values from the intersections, the conductivities were calculated with formula (4.12) and can be found in ***Table 3***.

**Table 3** Calculated values of the $\sigma_{DC}$-conductivities and the capacitances for the samples HK2 to HK5 using Cole-Cole plots.

| | HK2_2 | HK3_1 | HK4_3 | HK5_4 |
|---|---|---|---|---|
| **$\sigma_{DC}$, Cole-Cole plot, 200 °C [S/cm]** | 2.7E−07 | 2.8E−07 | 6.9E−12 | 7.6E−13 |
| **$\sigma_{DC}$, conductivity plot, 200 °C [S/cm]** | 2.7E−07 | 2.8E−07 | 6.9E−12 | no DC-plateau |
| **$C_{Cole\text{-}Cole\ plot}$ [pF]** | 11.5 | 9.5 | 12.9 | 11.4 |

For HK2 to HK4, the calculated $\sigma_{DC}$ values of the Cole-Cole plots correspond with the read-out $\sigma_{DC}$ values from the IS conductivity plots. For HK5, there was no *DC*-plateau present in the conductivity plot at 200 °C which could be compared to the corresponding Cole-Cole plot value.

Different regions in a ceramic are defined by their own resistance $R$ and capacitance $C$, which are usually placed in parallel. The product of $R$ and $C$ defines the characteristic relaxation time $\tau$ for each parallel $RC$ element

$$RC = \tau \quad (4.13)$$

$$\omega_{max} RC = 1 \quad (4.14)$$

The angular frequency at maximum loss ($\omega_{max}$) is defined by the relation

$$\omega_{max} = 2\pi\nu \quad (4.15)$$

with $\nu$ as the corresponding frequency at the maximum of the semicircle. In ***Fig. 4.8***, this is indicated by blue arrows.

The above formulas allow the calculation of the various RC elements for different regions in the probe [49]. By rearranging ( 4.14) and ( 4.15) to ( 4.16), the capacitances for each sample at 200 °C were calculated (see ***Table 3***).

$$C = \frac{1}{R(2\pi\nu)} \qquad (4.16)$$

Taking the picture of an idealized ceramic consisting of grains and grain boundaries (Brickwork model) allows the possible assignment of the calculated capacitances to the according regions in the sample. According to *Irvine et al*. [49], the ion transport of samples with capacitances of $10^{-12}\,F$, can be assigned to bulk ion transport. Capacitances between $10^{-11}$ to $10^{-8}$ F would be dedicated to grain boundaries. The capacitances for the samples HK2 to HK4, determined by the Cole-Cole plots (***Table 3***), are in the picofarad range ($10^{-12}\,F$) and can be assigned to bulk ion transport

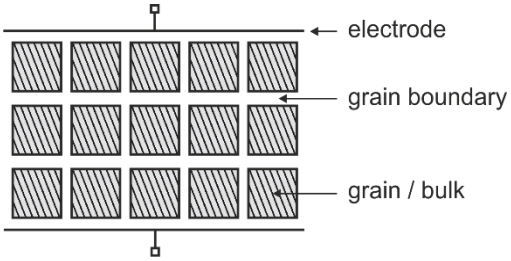


**Fig. 4.9** Scheme of the Brickwork model for grain and grain boundary regions in a ceramic sample between two metal electrodes according to [49].

The capacitance can be also calculated, by plotting the real part of the permittivity ($\varepsilon'$) against the frequency ($\nu$), which is illustrated exemplarily for HK2_2 in ***Fig. 4.10***.

The determined relative permittivity values from the plateaus were put in formula

$$C = \varepsilon'_{\mathrm{r}}\varepsilon_0\frac{A}{l} \qquad (4.17)$$

to calculate the capacitances. $\varepsilon_0$ stands for the permittivity in the vacuum (8.854 x $10^{-14}$ F $cm^{-1}$), $A$ and $l$ for the area of the sample and the thickness. To obtain a value for a unit cell constant, $\frac{A}{l} = 1\ cm^{-1}$ [49]. The calculated capacitances from the permittivity plots (***Fig. 4.10***) are presented in ***Table 4*** and have the same magnitude as the capacitances calculated from the Cole-Cole plots. Thus, it is assumed, that the recorded conductivity processes attributable to bulk phenomena.

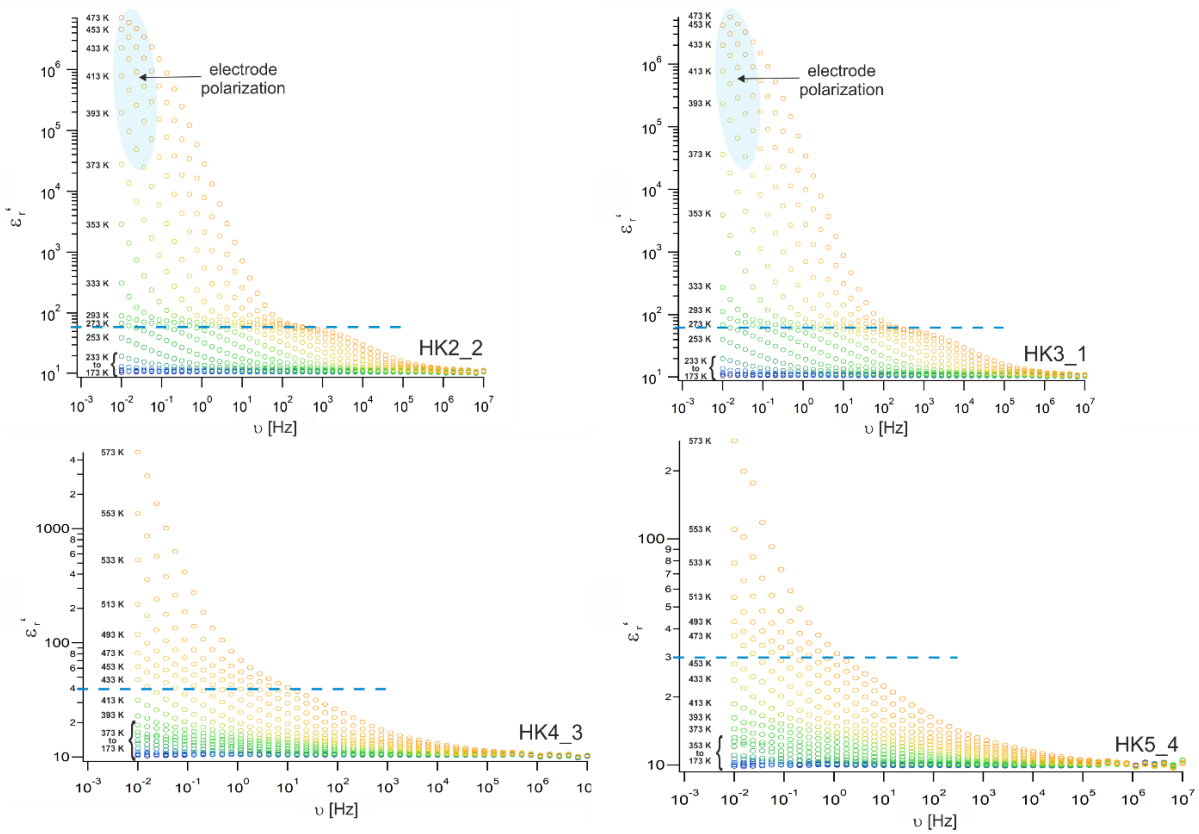


**Fig. 4.10** Permittivity plots for the samples HK2 – HK5. The relative permittivity $\varepsilon_r'$ is plotted against the frequency $\upsilon$. The blue dashed line marks the saddle points (plateaus) for each isotherm which allow to calculate the value for the temperature independent capacitance $C$. The plateau values from the permittivity plots correlate with the frequencies at maximum loss from the Cole-Cole plots (blue arrow). The blue marked areas indicate the electrode polarizations.

**Table 4** presents the calculated capacitances from the permittivity and Cole-Cole plot.

| | HK2_2 | HK3_1 | HK4_3 | HK5_4 |
|---|---|---|---|---|
| **$C_{\text{Permittivity plot}}$ [pF]** | 2.4 | 2.2 | 1.9 | 1.8 |
| **$C_{\text{Cole-Cole plot}}$ [pF]** | 11.5 | 9.5 | 12.9 | 11.4 |

## 4.3 Characterization of $BaLiF_3$ samples by nuclear magnetic resonance (NMR) spectroscopy

Further investigations of HK2 to HK5 were carried out by static $^{7}$Li and $^{19}$F NMR spectroscopy. Therefore, the samples were enclosed in glass capillaries under vacuum conditions. Exemplarily, the measured NMR spectra of HK2 between 253 K and 543 K are illustrated in ***Fig. 4.11***. Starting with the $^{7}$Li NMR spectra of HK2 under non-rotating conditions (a), one can see a single signal for each measured temperature ***Fig. 4.11***. Because of the cubic

symmetry of the $BaLiF_3$ lattice, quadrupole intensities are not present even though $^7$Li is a spin-$\frac{3}{2}$ nucleus [41].

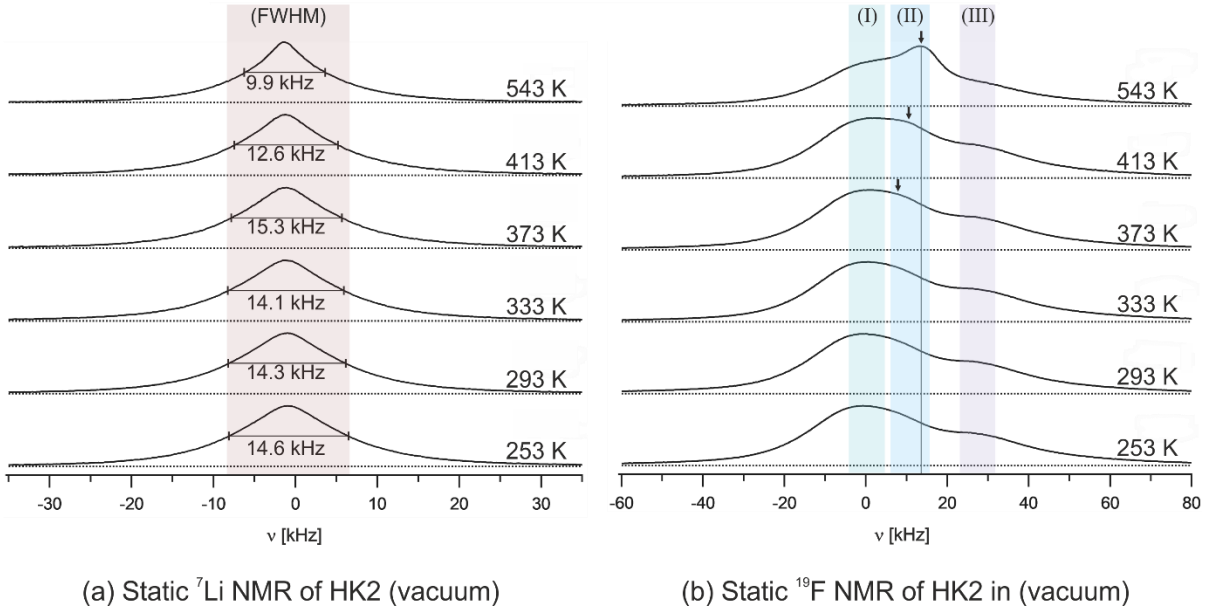


**Fig. 4.11** (a) Illustration of the recorded static $^7$Li NMR spectra of HK2 under vacuum conditions in a temperature range of 253 K to 543 K. The grey bar can be used as an optical assistance to compare the FWMHs in frequencies $\nu$. (b) Illustration of the recorded static $^{19}$F NMRs of HK2 under vacuum conditions in a temperature range of 253 K to 543 K. The bars (I – III) are indicating the positions for the supposed three intensity maxima. The intensities vary depending on the temperatures at which the sample was measured. The NMR spectra for HK3, HK4 and HK5 can be found in the annex (**Fig. C – E**).

For $^7$Li commencing at 253 K, a small narrowing can be seen towards elevated temperatures, in particular for temperatures above 400 K.

The broadening of the NMR lines at lower temperatures is a result of dipolar interactions between $^7$Li-$^7$Li and $^7$Li-$^{19}$F [41]. Additionally, the shape of the $^7$Li NMR lines, thus also the FWHMs, have a strong angular dependency towards the external magnetic field $\vec{B}_0$. This is induced by nuclear dipolar fields from neighboring nuclei in the samples. In a powder sample, the crystallites are randomly orientated, which will lead to a variety of overlapping signals and thus to an additional line broadening in the NMR spectra [50]. With an increasing temperature, molecular motion (Brownian motion) rises. This leads to a reduction of dipole-dipole interactions which results in decreased FWHMs.

The $^7$Li NMR lines of all samples at 293 K and 543 K are illustrated in ***Fig. 4.12*** (a). As already mentioned, the peak narrowing from 293 K to 543 K is only observable with HK2 and HK3. This could be explained with the work of *Goto et al.* [50], which connects random orientation of the crystallites towards an external magnetic field $\vec{B}_0$ with a superposition of the individual NMR lines. The growth of the crystallites during the 24 h annealing process,

probably led to an overall higher orientated crystallite system with much more narrow NMR lines, compared to the milled and disordered systems HK2 and HK3. To see, if a crystallite growth for HK2 and HK3, analogous to the intentional 24 h heat-treatment took accidently place during the NMR measurement at 543 K, a second NMR measurement at 293 K followed by an XRPD measurement would have been necessary.

Narrowing for HK2 and HK3 is traced back to an increased Li ion diffusivity at elevated temperatures.

The $^{19}$F NMR spectra of HK2 recorded under non-rotating and vacuum conditions are illustrated in ***Fig. 4.11*** (b). For the temperature range between 253 K to 333 K, only two maxima can be indicated for the NMR lines, present in the sections (I) and (III). A third maximum in section (II) becomes first visible at 373 K and develops with an increasing temperature. Since the intensities of the three maxima vary with the temperature for each measurement, it was not possible to mark the FWHMs for the $^{19}$F NMR lines. Comparing the FWHMs of the fluorine NMR might give little information, as in contrast to the $^{7}$Li NMR lines, the angular dependence of the FWHM at the $^{19}$F site is weak [50].

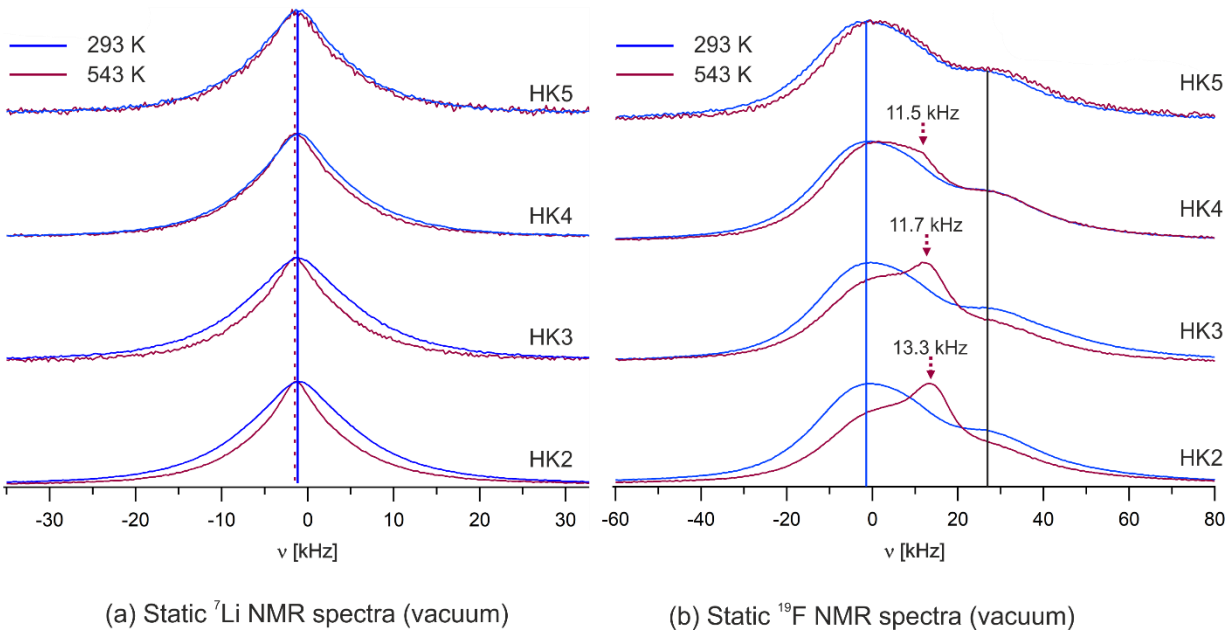


**Fig. 4.12** (a) Illustration of the recorded static $^{7}$Li NMR spectra of HK2 / HK3 (blue) and HK4 / HK5 (black) for 293 K (solid lines) and 543 K (dashed lines) under vacuum conditions. The vertical solid (293 K) line and the vertical dashed line (543 K) mark the range of the resonance maxima (b) Illustration of the recorded static $^{19}$F NMR spectra of HK2 / HK3 (blue) and HK4 / HK5 (black) for 293 K (solid lines) and 543 K (dashed lines) under vacuum conditions. The two vertical solid lines (293 K) mark the range of the resonance maxima. The dashed arrows indicate the positions of the various peak maxima at 543 K.

Due to the fact, that $BaLiF_3$ was synthesized via high energy ball milling, structural disorder was introduced into the measured system. The shape of the $^{19}F$ NMR line at low temperatures might be the result of various domains of magnetically different $F^-$ species which lead to a superposition of intensities. With increasing temperatures, the resonance maxima from section (II) emerge for almost all samples as a consequence of averaging dipole-dipole interactions, as well as local chemical shift interactions of the magnetically inequivalent $F^-$ ions. Thus, the mean exchange rate increases, slows down the spin-spin relaxation and leads to a signal narrowing [51].

The $^{19}F$ NMR lines of all samples at 293 K and 543 K are illustrated in ***Fig. 4.12*** (b). At room temperature, the NMR lines of the samples HK2 to HK5 look similar. For the non-tempered samples at 543 K, the signal shape is modified and a new maximum arises, indicated by the red dashed arrows. For HK4, the resonance maximum is still partly visible at the NMR line but the new maximum seems to degenerate again because of the sintering process.

The resonance intensity is connected with the $F^-$ conductivity in the sample. The heat-treatment of HK4 and HK5 has increased the mean crystallite size, thus leading to a lowered ionic conductivity and less intense NMR lines in the spectra.

The resonance maximum is not visible for HK5 at 543 K. As already mentioned in other parts of this work, the annealed samples HK4 and HK5 show different characteristics even if their precursors have almost identical properties. This can be probably attributed to the various ball-to-powder ratios during the milling process. The result could be different $BaLiF_3$ domains which might have influenced the crystallite growth and thus the fluoride conductivity.

Finally, a third main resonance maximum (black solid line) is present in ***Fig. 4.12***. A major change between the NMR lines for the two illustrated temperatures can be seen for HK2 and HK3. With an increasing temperature, the intensity of the maximum is reduced. For the NMR measurement of HK4 and HK5, there is no difference between the $^{19}F$ NMR lines in section (III).

# 5 Conclusion

$BaLiF_3$ is a rare representative of lithium and fluoride containing ceramics, crystallizing in anti-perovskite structure. Within this diploma thesis, it was synthesized in two different ways by joint high energy ball milling of stoichiometric mixtures of $BaF_2$ and LiF. The milling processes yielded $BaLiF_3$ nano-crystallites with an average diameter of 15 nm. Subsequently, the products were tempered at 870 K for 24 h to compare the effect of the heat-treatment on the sample properties. The annealing increased the mean crystallite size of the samples HK4 and HK5. The samples were kept in an argon atmosphere to prevent contamination

Employing XRPD revealed, that for HK2 and HK3 $BaLiF_3$ with an amorphous fraction was synthesized. Heat-treating the samples yielded HK4 and HK5 with an increased mean crystallite size. IS investigation determined, that there was no difference in the activation energies and the magnitude of the DC-conductivities for the milled samples. The heat-treatment induced a healing process of the structural disordered samples, leading to enlarged crystallites and thus to rising activation energies. For the tempered samples HK4 and HK5, the DC-conductivities decreased compared to their precursors. Despite congruent values for the obtained data of the non-tempered samples, a clearly visible difference was measured between the heat-treated ones. The samples were identically treated, however, the different ball-to-powder ratios and milling times during the mechanochemical preparation of HK2 and HK3 will have resulted in divergent initial conditions for the annealing process. According to *Irvine et al*. [49], the determined capacitances with a magnitude of 1.2 to 12.9 pF can be assigned to bulk ion transport.

The diffusion parameters for $^7Li$ and $^{19}F$ between 253 K and 543 K were also studied, on the basis of static solid-state NMR spectroscopy. Comparing measurements at low and elevated temperatures, there was just a small narrowing within the single $^7Li$ NMR lines visible. In contrast to that, the three resonance maxima in the $^{19}F$ NMR lines vary strongly as a function of the $F^-$ conductivity, ergo as a function of the applied temperatures and the dislocation density.

For a better understanding of the sample properties, further investigations via dynamic nuclear magnetic resonance could be performed. Moreover, heat-treating $BaLiF_3$ samples at various temperatures, followed by subsequent XRD, IS and NMR measurements, are suggested.

# 6 Appendix

**Table I** Composition of the milled BaF2 and LiF mixture for HK1 and HK2.

| Compounds | m [g] | M [g/mol] | n [mol] |
|---|---|---|---|
| **$BaF_2$** | 8.766 | 175.324 | 0.0500 |
| **LiF** | 1.297 | 25.939 | 0.0500 |
| **$BaLiF_3$** | 10.063 | 201.260 | 0.0500 |

**Table II** Composition of the milled $BaF_2$ and LiF mixture for HK3.

| Compounds | m [g] | M [g/mol] | n [mol] |
|---|---|---|---|
| **$BaF_2$** | 1.742 | 175.324 | 0.00994 |
| **LiF** | 0.258 | 25.939 | 0.00994 |
| **$BaLiF_3$** | 2.000 | 201.260 | 0.00994 |

**Table III** Pressing parameters for the impedance pallets. The pallets marked * withstood the preparation procedures and were used for the impedance measurement.

| Sample | m [mg] | Diameter [mm] | $t_{pressing}$ [min] | pressure [t] | Thickness [mm] |
|---|---|---|---|---|---|
| HK2_1 | 60 | 5.0 | 5 | 0.5 | - |
| ***HK2_2** | **60** | **5.00** | **5** | **0.5** | **0.89** |
| ***HK3_1** | **60** | **5.00** | **5** | **0.5** | **0.90** |
| HK3_2 | 60 | 5.00 | 5 | 0.5 | - |
| ***HK4_1** | **60** | **5.00** | **5** | **0.5** | **0.88** |
| HK4_2 | 60 | 5.00 | 5 | 0.5 | - |
| ***HK4_3** | **70** | **5.00** | **7** | **0.5** | **1.01** |
| HK5_1 | 60 | 5.00 | 5 | 0.5 | - |
| HK5_2 | 60 | 5.00 | 5 | 0.5 | - |
| ***HK5_3** | **60** | **5.00** | **6** | **0.5** | **0.90** |
| ***HK5_4** | **70** | **5.00** | **7** | **0.5** | **0.98** |

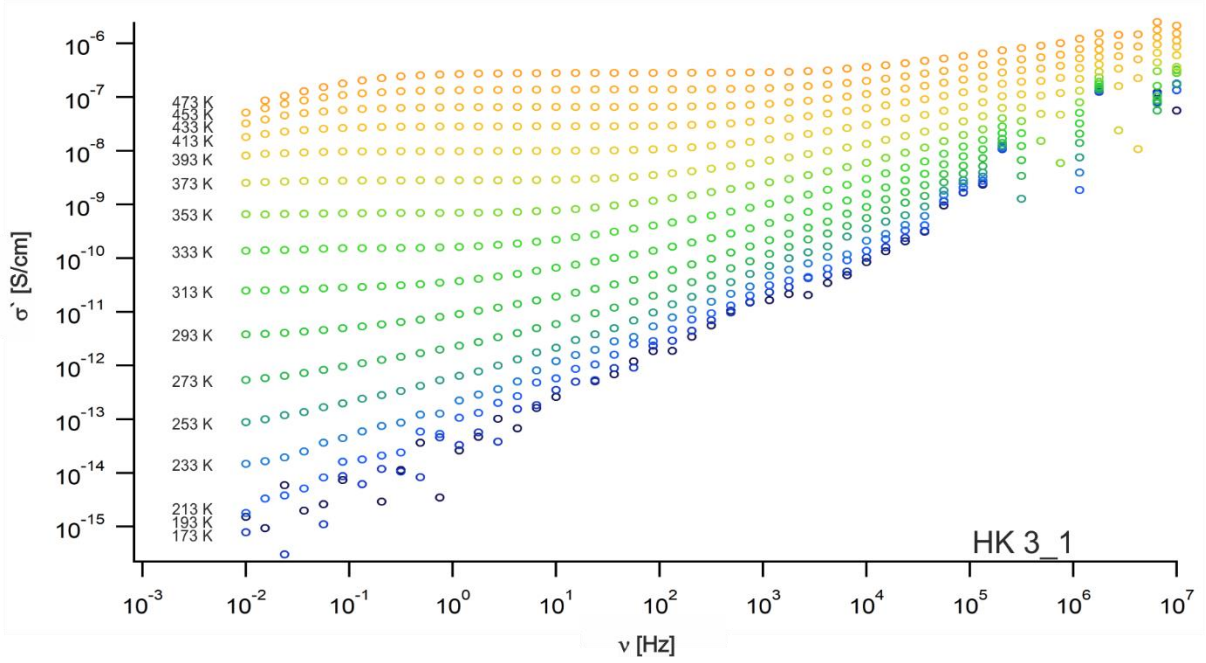


**Fig. A** Conductivity plot of sample HK3_1 from the impedance measurement. The logarithmic real part of the conductivity $\sigma'$ is plotted against the logarithmic frequency $\nu$.

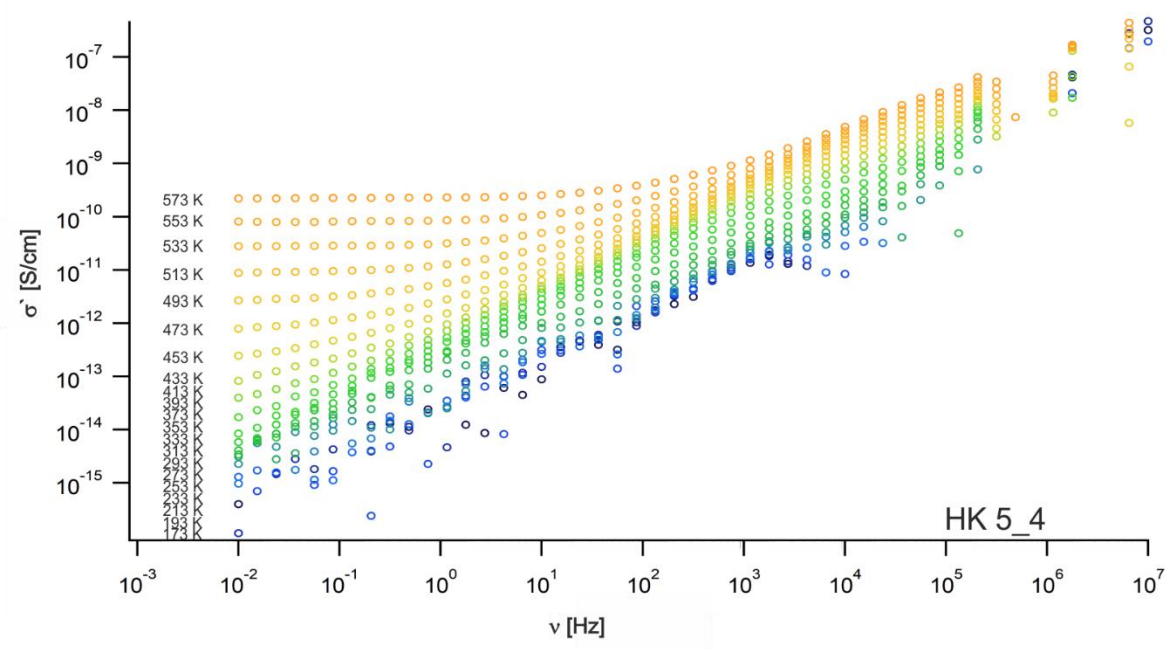


**Fig. B** Conductivity plot of sample HK5_4 from the impedance measurement. The logarithmic real part of the conductivity $\sigma'$ is plotted against the logarithmic frequency $\nu$.

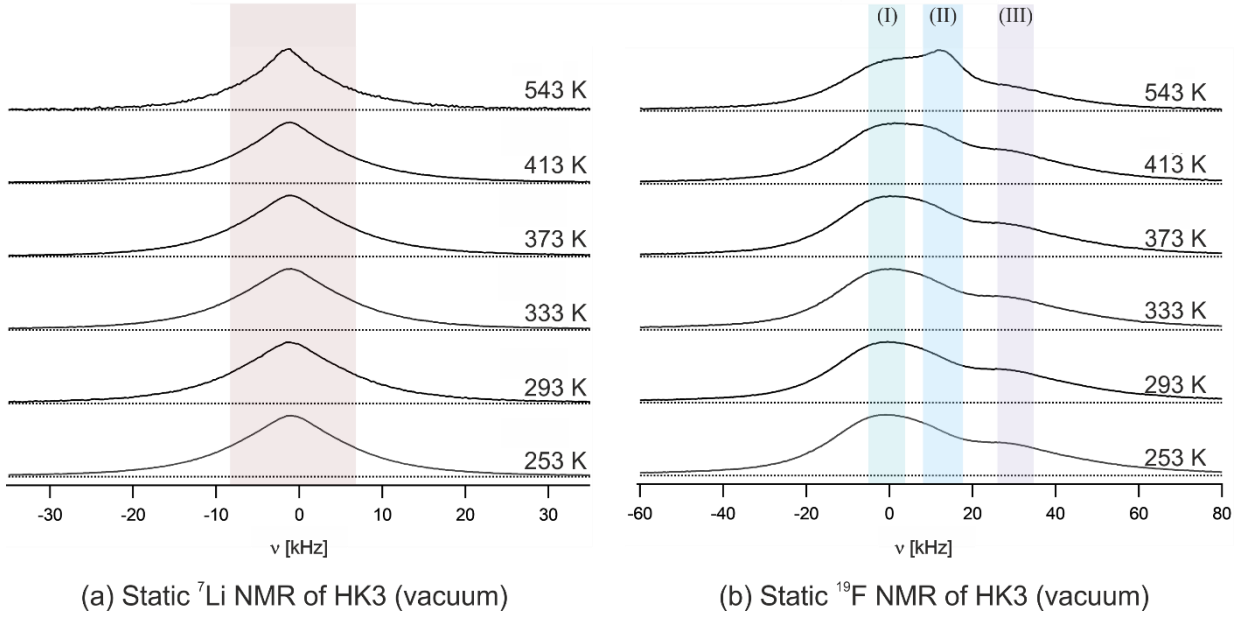


**Fig. C** (a) Illustration of the recorded static $^{7}$Li NMR spectra of HK3 under vacuum conditions in a temperature range of 253 K to 543 K. The grey bar can be used as an optical assistance to compare the FWMHs in frequencies $\nu$. (b) Illustration of the recorded static $^{19}$F NMRs of HK3 under vacuum conditions in a temperature range of 253 K to 543 K. The bars (I – III) are indicating the positions for the supposed three intensity maxima. The intensities vary depending on the temperatures at which the sample was measured.

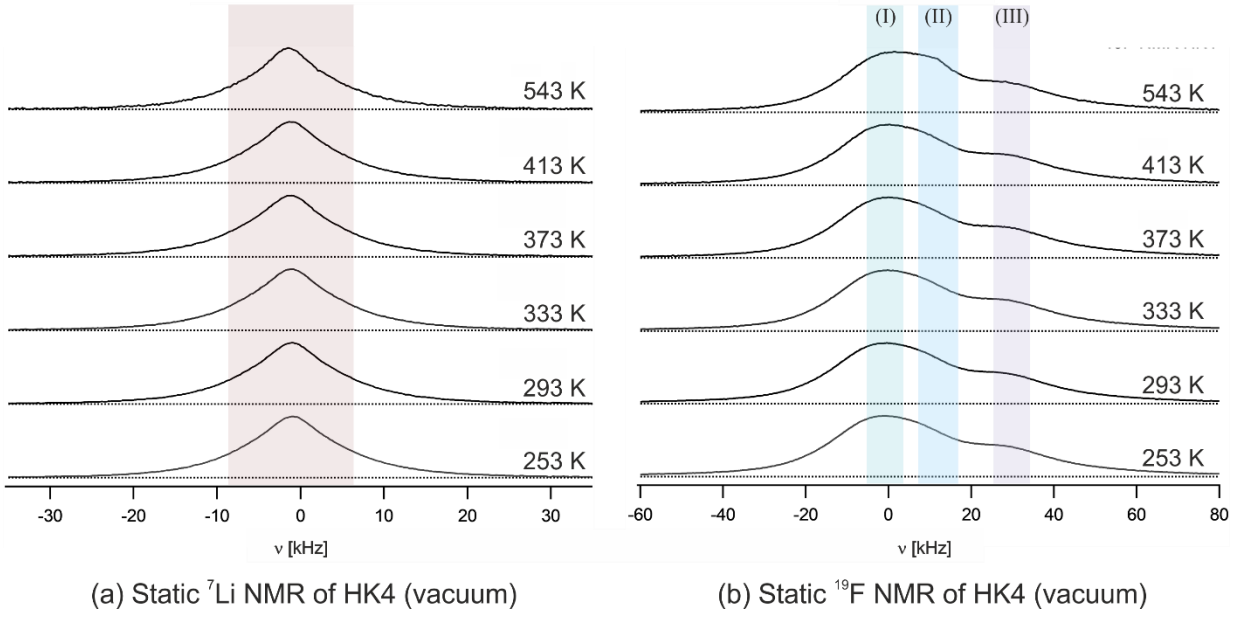


**Fig. D** (a) Illustration of the recorded static 7Li NMR spectra of HK4 under vacuum conditions in a temperature range of 253 K to 543 K. The grey bar can be used as an optical assistance to compare the FWMHs in frequencies $\nu$. (b) Illustration of the recorded static $^{19}$F NMRs of HK4 under vacuum conditions in a temperature range of 253 K to 543 K. The bars (I – III) are indicating the positions for the supposed three intensity maxima. The intensities vary depending on the temperatures at which the sample was measured.

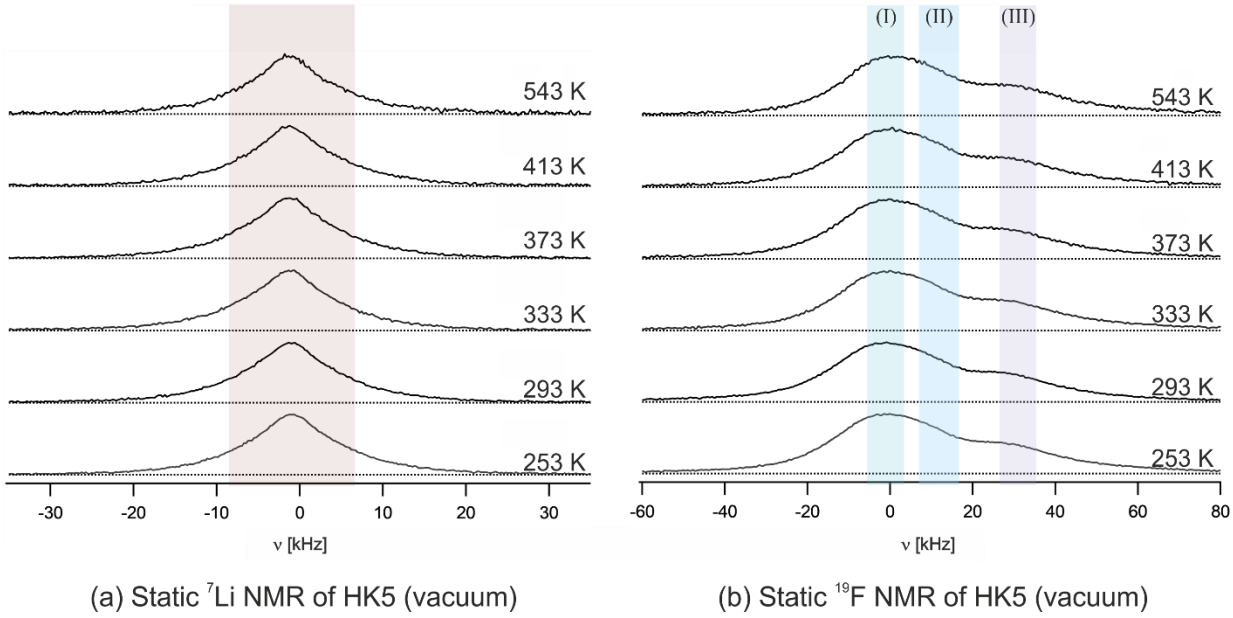


(a) Static $^{7}$Li NMR of HK5 (vacuum) (b) Static $^{19}$F NMR of HK5 (vacuum)

**Fig. E** (a) Illustration of the recorded static $^{7}$Li NMR spectra of HK5 under vacuum conditions in a temperature range of 253 K to 543 K. The grey bar can be used as an optical assistance to compare the FWMHs in frequencies $\nu$. (b) Illustration of the recorded static $^{19}$F NMRs of HK3 under vacuum conditions in a temperature range of 253 K to 543 K. The bars (I – III) are indicating the positions for the supposed three intensity maxima. The intensities vary depending on the temperatures at which the sample was measured.

# 7 References


[1] Whittingham, M.S.: Lithium Batteries and Cathode Materials. *Chem. Rev.*, **104** (10), 2004, p. 4271–4302.

[2] Yang, P. et al.: Electrochromic energy storage devices. *Mater. Today*, **19** (7), 2016, p. 394–402.

[3] Tarascon, J.-M., Armand, M.: Issues and challenges facing rechargeable lithium batteries. *Nature*, **414** (6861), 2001, p. 359–367.

[4] Kamaya, N. et al.: A lithium superionic conductor. *Nat Mater*, **10** (9), 2011, p. 682–686.

[5] Armand, M., Tarascon, J.-M.: Building better batteries. *Nature*, **451** (7179), 2008, p. 652–657.

[6] Wang, Y. et al.: Design principles for solid-state lithium superionic conductors. *Nat Mater*, **14** (August), 2015, p. 1–23.

[7] Düvel, A. et al.: Mechanosynthesis of the Fast Fluoride Ion Conductor Ba1−xLaxF2+x: From the Fluorite to the Tysonite Structure. *J. Phys. Chem. C*, **118**, 2014, p. 7117–7129.

[8] Rongeat, C. et al.: Solid Electrolytes for Fluoride Ion Batteries: Ionic Conductivity in Polycrystalline Tysonite-Type Fluorides. *ACS Appl. Mater. Interfaces*, **6** (3), 2014, p. 2103–2110.

[9] Hull, S.: Superionics: crystal structures and conduction processes. *Reports Prog. Phys.*, **67** (7), 2004, p. 1233–1314.

[10] Ahmad, M.M. et al.: Dielectric relaxation properties of Pb1-xSnxF2 solid solutions prepared by mechanochemical milling. *J. Phys. D. Appl. Phys.*, **40** (19), 2007, p. 6020–6025.

[11] Suryanarayana, C.: Mechanical alloying and milling. *Prog. Mater. Sci.*, **46** (1–2), 2001, p. 1–184.

[12] Düvel, A. et al.: Mechanosynthesized nanocrystalline BaLiF(3): The impact of grain boundaries and structural disorder on ionic transport. *Phys. Chem. Chem. Phys.*, **12** (37), 2010, p. 11251–11262.

[13] Kirkwood, J.G. et al.: Flow Equations and Frames of Reference for Isothermal Diffusion in Liquids. *J. Chem. Phys.*, **33** (5), 1960, p. 1505–1513.

[14] Preishuber-Pflügl, F., Wilkening, M.: *Mechanochemically Synthesized Fluorides: Local Structures and Ion Transport*. Graz University of Technology, 2016.

[15] Habasaki, J. et al.: *Dynamics of Glassy, Crystalline and Liquid Ionic Conductors*. 2017.

[16] Mehrer, H.: *Diffusion in solids: Fundamentals, methods, materials, diffusion-controlled processes*. Springer Berlin Heidelberg, 2007.

[17] Moore, E.A., Smart, L.E.: *Solid State Chemistry: An Introduction, Fourth Edition*. CRC Press, 2012.

[18] Borchardt-Ott, W.: *Kristallographie: Eine Einführung für Naturwissenschaftler*.

Springer-Verlag Berlin Heidelberg, 2009.

[19] Kittel, C., Kroemer, H.: *Thermal Physics*. W. H. Freeman, 1980.

[20] Martin, A. et al.: *Einführung in die Festkörperchemie*. Springer Berlin Heidelberg, 2000.

[21] Kraftmakher, Y.: Equilibrium vacancies and thermophysical properties of metals. *Phys. Rep.*, **299** (2–3), 1998, p. 79–188.

[22] Callister, W.D., Rethwisch, D.G.: *Fundamentals of Materials Science and Engineering: An Integrated Approach*. John Wiley & Sons, 2012.

[23] Rack, P.D.: *Introduction To Materials Science For Engineers*. Pearson, 2003.

[24] Cullity, B.D., Stock., S.R.: *Elements of X-Ray Diffraction*. Addison-Wesley Publishing Company, Inc., 1956.

[25] Holzwarth, U., Gibson, N.: The Scherrer equation versus the 'Debye-Scherrer equation'. *Nat. Nanotechnol.*, **6** (9), 2011, p. 534–534.

[26] Izumi, F., Ikeda, T.: *Implementation of the Williamson – Hall and Halder – Wagner Methods into RIETAN-FP*. 2014.

[27] Barsoukov, E., Macdonald, J.R.: *Impedance Spectroscopy*. Wiley & Sons, 2005.

[28] Saikia, S.J. et al.: Implementation of Ohm's Law using MATLAB Simulink. *IJISET*, **1** (3), 2014, p. 289–291.

[29] Lvovich, V.F.: *Applications to Electrochemical and Dielectric Phenomena*. John Wiley & Sons, 2012.

[30] Conway, B.E.: *Electrochemical Supercapacitors: Scientific Fundamentals and Technological Applications*. Springer US, 1999.

[31] Sidebottom, D.L.: Colloquium: Understanding ion motion in disordered solids from impedance spectroscopy scaling. *Rev. Mod. Phys.*, **81** (3), 2009, p. 999–1014.

[32] Breuer, S. et al.: Separating bulk from grain boundary Li ion conductivity in the sol – gel prepared solid. **5**, 2015.

[33] Roling, B. et al.: Ionic ac and dc conductivities of glasses with varying modifier content. *J. Non. Cryst. Solids*, **226** (138–144), 1998.

[34] Barsoukov, E., Macdonald, R.J.: *Impedance Spectroscopy Theory, Experiment and Applications*. 2010.

[35] Duer, M.J.: *Introduction to Solid-State NMR Spectroscopy*. Blackwell Science, 2002.

[36] Vij, D.R.: *Handbook of Applied Solid State Spectroscopy*. Springer US, 2006.

[37] Levitt, M.H.: *Spin Dynamics: Basics of Nuclear Magnetic Resonance*. John Wiley & Sons, 2008.

[38] Bloch, F.: Nuclear induction. *Phys. Rev.*, **70** (7–8), 1946, p. 460–474.

[39] Bloch, F. et al.: The Nuclear Induction Experiment. *Phys. Rev.*, **70** (7–8), 1946, p. 474–485.

[40] Balzar, D.: X-Ray Diffraction Line Broadening. Modeling and Applications to High-Tc

Superconductor. *J. Res. Natl. Inst. Stand. Technol.*, **98** (3), 1998, p. 321–353.

[41] Düvel, A. et al.: Ion conduction and dynamics in mechanosynthesized nanocrystalline BaLiF3. *Solid State Ionics*, **184** (1), 2011, p. 65–69.

[42] Wall, C.: *Mangan-Nickel-und Cobaltverbindungen als Konversionselektrodenmaterialien für Lithium-Ionen-Batterien*. Darmstadt University of Technology, 2014.

[43] Bensalah, A. et al.: Growth and characterization of BaLiF3 single crystal as a new optical material in the VUV region. *J. Alloys Compd.*, **348** (1–2), 2003, p. 258–262.

[44] Jonscher, A.K.: The 'universal' dielectric response. *Nature*, **267** (5613), 1977, p. 673–679.

[45] Wohlmuth, D. et al.: Order vs. disorder—a huge increase in ionic conductivity of nanocrystalline LiAlO2 embedded in an amorphous-like matrix of lithium aluminate. *J. Mater. Chem. A*, **2** (47), 2014, p. 20295–20306.

[46] Patro, L.N., Hariharan, K.: Influence of synthesis methodology on the ionic transport properties of BaSnF4. *Mater. Res. Bull.*, **46** (5), 2011, p. 732–737.

[47] Heitjans, P., Indris, S.: Diffusion and ionic conduction in oxide glasses. *J. Phys. Condens. Matter*, **15** (1), 2003, p. R1257–R1289.

[48] Patro, L.N., Hariharan, K.: Mechanical milling: An alternative approach for enhancing the conductivity of SnF2. *Mater. Lett.*, **80**, 2012, p. 26–28.

[49] Irvine, J.T.S. et al.: Electroceramics: Characterization by Impedance Spectroscopy. *Adv. Mater.*, **2** (3), 1990, p. 132–138.

[50] Goto, A. et al.: Investigation for the possible crystal NMR quantum computing device with BaLiF3. *Phys. B Phys. Condens. Matter*, **298** (1–4), 2001, p. 585–589.

[51] Ruprecht, B. et al.: High anion conductivity in a ternary non-equilibrium phase of BaF2 and CaF2 with mixed cations. *Phys. Chem. Chem. Phys.*, **11** (17), 2009, p. 3071–3081.

[52] Singh, V.S. et al.: Wet chemical synthesis of LiBaF3 phosphor. *J. Alloys Compd.*, **579**, 2013, p. 165–168.

[53] Porter, D.A., Easterling, K.E.: *Phase Transformations in Metals and Alloys*. 1992.

[54] Preishuber-Pflügl, F. et al.: Evidence of low dimensional ion transport in mechanosynthesized nanocrystalline BaMgF4. *Dalt. Trans.*, **43** (26), 2014, p. 9901–9908.